minerals

MDPI

Article

Genetic Model Variability of Deep-Sea Phosphorites Along the Iberian–North African Margins Evidenced by In Situ Geochemistry and Isotopic Signatures

Sophie Decrée [1,2,*], Francisco Javier González [3], Egidio Marino [3], Esther Santofimia [3], Vitor Hugo Magalhães [4,5], Nolwenn Coint [6], Eduardo Teixeira Mansur [6], Jean-Marc Baele [7] and Etienne Deloule [8]

1 Institute of Natural Sciences, Geological Survey of Belgium, 29, rue Vautier, B-1000 Brussels, Belgium
2 The Mineral Resources Expert Group (MREG), EuroGeoSurveys, B-1000 Brussels, Belgium
3 Marine Geology Resources and Extreme Environments, Geological Survey of Spain (IGME-CSIC), Ríos Rosas, 23, 28003 Madrid, Spain; fj.gonzalez@igme.es (F.J.G.); e.marino@igme.es (E.M.); e.santofimia@igme.es (E.S.)
4 Marine Geology and Georesources Division, Portuguese Institute for Sea and Atmosphere—IPMA, 1749-077 Lisbon, Portugal; vitor.magalhaes@ipma.pt
5 Instituto Dom Luiz, Faculty of Sciences, University of Lisbon, 1749-016 Lisbon, Portugal
6 Norwegian Geological Survey, 7040 Trondheim, Norway; nolwenn.coint@ngu.no (N.C.); eduardo.teixeira.mansur@ngu.no (E.T.M.)
7 Department of Geology and Applied Geology, University of Mons, 9, rue de Houdain, B-5000 Mons, Belgium; jean-marc.baele@umons.ac.be
8 Université de Lorraine, CNRS, CRPG, 15, rue Notre-Dame des Pauvres, F-54500 Vandoeuvre-les-Nancy, France; etienne.deloule@univ-lorraine.fr
* Correspondence: sophie.decree@naturalsciences.be

Abstract

Phosphorites are a vital source of phosphorus for agricultural and industrial applications and are increasingly recognized for their potential as secondary repositories of critical raw materials (CRMs) such as rare earth elements plus yttrium (REYs). This study investigates deep-sea phosphorites from the Galicia Bank, Madeira, and Canary Seamounts, in the NE Atlantic Ocean, which are spatially associated with ferromanganese (Fe-Mn) mineralization. Through integrated petrographic, geochemical, and in situ isotopic analyses (O and Sr), we assess the timing, processes, and paleoenvironmental conditions of phosphogenesis and its implications for CRM enrichment. Rare earth element patterns in apatite reflect a predominant seawater-derived signature with variable Ce anomalies. Nevertheless, variable Y/Ho ratios point to evolving fluid sources including a hydrogenous component (directly derived from seawater), modified porewaters and, locally, volcanic or possibly hydrothermal inputs. Oxygen and strontium isotope compositions constrain phosphogenesis to several episodes ranging from the Upper Cretaceous to the Middle Miocene, with distinct isotopic shifts identifying both primary formation and later overprinting processes mostly linked to Fe-Mn oxyhydroxide growth or volcanic–hydrothermal activity. These findings highlight the dynamic and multiphase nature of phosphorite formation in deep-marine settings. The integration of high-resolution geochemical and isotopic tools proves essential for reconstructing genetic histories, defining metallogenic context and evaluating CRM prospectivity in complex submarine systems.

Keywords: Galicia Bank; Tropic Seamount; Seine Seamount; phosphorite; phosphogenesis; apatite; post-depositional processes; rare earth elements; Sr and O isotopes

Academic Editor: Hermann Kudrass

Received: 30 April 2026
Revised: 8 June 2026
Accepted: 20 June 2026
Published: 22 June 2026

1. Introduction

Phosphorus is a vital element for the growth and development of all living organisms. It is primarily found in the form of apatite, particularly in sedimentary marine phosphorites [1]. The largest share of extracted phosphorus is used for fertilizer production (around 82% of global production), which is crucial to meet the increasing demand for food driven by global population growth. Europe, which relies heavily on imports, annually brings in approximately 4 million tonnes of phosphate-rich material [2]. Given its importance, phosphate rock was officially designated as a critical raw material (CRM) by the European Union in 2014 [3], recognizing its essential role in modern technologies, the green energy transition, and defense applications [2]. Recently, phosphate deposits have gained even more attention because of their potential as a source of other CRMs, including fluorine (F) and rare earth elements plus yttrium (REYs) [4–7] (Christmann, 2014; Ihlen et al., 2014; Emsbo et al., 2015; Decrée et al., 2022). Notably, apatite deposits—whether sedimentary or igneous in origin—are seen as a key source for rare earth elements (REEs) as a by-product of apatite itself, offering a significant advantage: their easier extraction compared to traditional REE deposits [6,8]. The majority of global phosphorus production—approximately 80%—is derived from sedimentary phosphate deposits, primarily located in North Africa, China, the Middle East, South Africa, the United States, and Russia. Major sedimentary phosphate-related REE resources are classically associated with large shallow-marine phosphorite provinces developed along the southern Tethyan margin, including Morocco, West Sahara, Tunisia–Algeria, and Egypt. Phosphogenesis occurred during Upper Cretaceous–Eocene events under upwelling-controlled conditions and extensive shelf sedimentation [9–11]. Igneous apatite deposits also contribute to global phosphorus supply, although to a lesser extent [2]. In addition to these well-established sources, other sedimentary phosphorite deposits with economic potential have been identified on the continental shelves of the Atlantic, Pacific, and Indian Oceans [12–14]. Increasing attention is being directed toward these deep-sea resources, which represent a strategic opportunity to diversify the supply of CRM, supported by national and international initiatives and projects that promote their exploration, mapping, and extraction in a responsible and sustainable way [15–17]. In addition, deep-sea phosphorite deposits are commonly found alongside Fe-Mn mineralization in various regions [18–20]. The episodic occurrence of phosphatization during the growth of Fe-Mn crusts could play a critical role in modifying both their mineralogical and geochemical signatures [21–23]. Indeed, the formation of carbonate fluorapatite under suboxic conditions can lead to the partial dissolution of Mn oxides. This process may significantly influence the distribution and enrichment of CRMs, such as Co, Ni, Cu, Pt, REEs, and other elements, which are typically hosted in Mn-oxide phases [24–26]. The replacement of Mn oxides by apatite alters its capacity to retain or adsorb trace metals, whereas redox fluctuations associated with phosphogenesis may further redistribute CRM within the crust. Understanding these transformations is essential for interpreting the CRM potential of ferromanganese deposits and evaluating the post-depositional processes that control their economic value.

Due to its intrinsic significance as a potential economic source of CRM and the potential impact of its genesis on spatially associated ferromanganese oxyhydroxides, a comprehensive understanding of phosphorite formation is essential. This includes constraining its age, quantifying CRM concentrations, and characterizing the spatial distribution of these elements within the phosphorites. Mineralogy and geochemistry provide crucial information about the conditions that control the genesis of these deposits and help constrain the sedimentological and paleoceanographic settings in which phosphorite forms. The REE content and distribution in apatite give information about the environment during early diagenesis. The latter would be the preferential time for REE uptake of francolite (carbonate–fluorapatite), which is the dominant apatite type in phosphorite [27–29].

https://doi.org/10.3390/min16060661

Hence, REE enrichment in phosphorites cannot be interpreted solely as a seawater signature but may also reflect biological productivity, early diagenetic remobilization and mineral replacement processes [30–32]. Newly developed high-resolution tools—as in situ O and Sr isotope measurements on apatite—are helpful in deciphering the complex history of phosphogenesis [27,33–35]. The integration of high-resolution trace element data with isotopic signatures aims to reconstruct the timing and mechanisms of phosphogenesis in phosphorites, evaluate the role of post-depositional reworking and interaction with Fe–Mn mineralization, and assess the controls governing REY and CRM enrichment in contrasting depositional settings.

This study presents a petrographic and geochemical analysis of apatite from deep-sea phosphorites of varying ages, spatially associated with ferromanganese nodules and crusts from the Madeira and Canary seamounts, as well as the Galicia Bank, in the NE Atlantic Ocean (Figure 1).

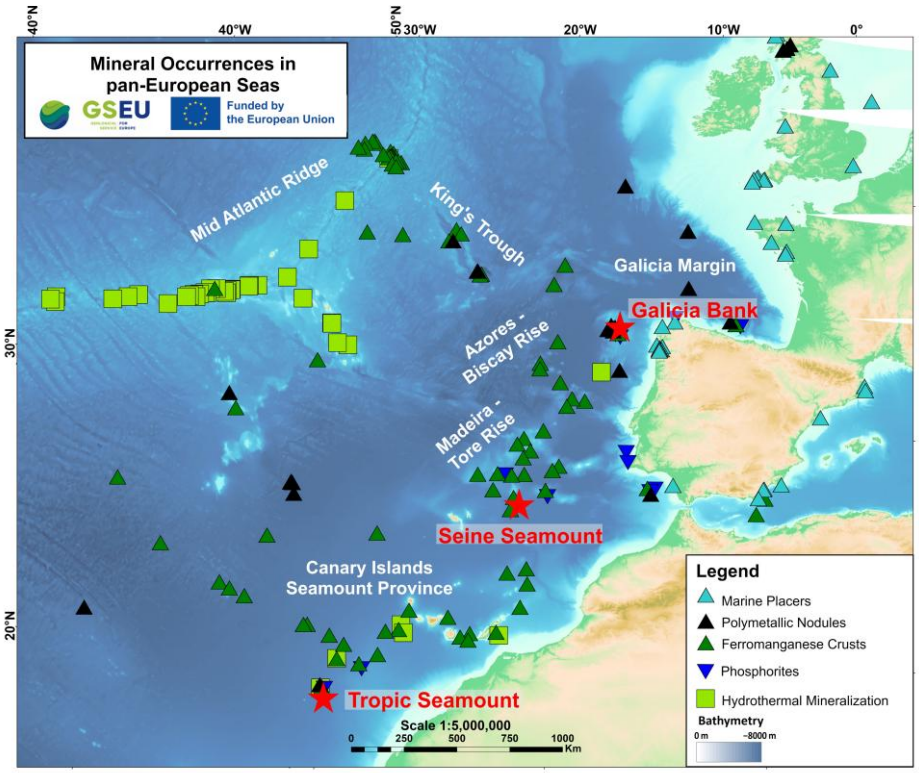

Figure 1. Provenance of the studied phosphorites (indicated by a star). The map of mineral occurrences in pan-European seas is modified after González et al. [36].

Prior to in situ analyses, imaging and spectroscopic techniques (scanning electron microscopy (SEM), cathodoluminescence (CL), laser-induced breakdown spectroscopy (LIBS)) revealed significant textural and chemical heterogeneity in apatite, guiding targeted investigations using electron probe micro-analysis (EPMA), laser ablation inductively coupled plasma mass spectrometry (LA-ICPMS, for trace elements and Sr isotopes), and secondary ion mass spectrometry (SIMS, for O isotopes). The studied phosphorites span a broad temporal range, from the Upper Cretaceous–Early Paleogene to the Lower Miocene, and likely formed under different paleoenvironmental conditions. By comparing these distinct settings, this study aims to assess whether variations in depositional environments are reflected in differences in CRM concentrations within the phosphorites, while also shedding light on major phosphogenic episodes during the late Mesozoic and the Cenozoic [35,37–41]. The Late Cretaceous phosphogenic episode is prominently recorded in the Tethyan sequences [35,41,42]. Phosphorites from this period are typically

associated with condensed sedimentation, characterized by intervals of sediment starvation that promote bioturbation and the formation of hardgrounds [41]. Most of them were formed during the evolution of the Neo-Tethys Ocean cycle in passive margins [42]. One of the main drivers of phosphogenesis during this time is believed to be the influence of upwelled waters enriched in phosphorus [35]. Paleogene phosphorite deposits are thought to develop in shallow marine settings such as inner continental shelves or epeiric seas [38,43], under conditions comparable to Late Cretaceous phosphogenesis, where upwelling of phosphorus-rich waters played a crucial role [35,41]. During the Neogene, major phosphogenesis events produced extensive phosphorites across regions such as the Mediterranean, the Middle East, South America, and coastal North America [44]. These events are generally linked to high sea levels and active upwelling in marginal basins, facilitated by favorable sedimentological conditions [35].

2. Geological Context

Three phosphorite sites have been studied. The samples investigated are presented in Figure 1 and Table 1.

Table 1. Brief description of the samples investigated in this study.

Sample Studied	Origin of the Sample (Institute, Museum)	Zone	Short Description	Previous Inferred Phosphatization Age	Considered Phosphorite Age in This Study (See Section 5)
ARTABRIA II-36DRN	IGME-CSIC	Galicia Bank	Layered phosphorite	Late Oligocene or Early Miocene [20]	Late Oligocene or Early Miocene [20]
ARTABRIA II-81DRR	IGME-CSIC	Galicia Bank	Phosphorite serving as substrate for Fe-Mn nodules		
3521-6	IPMA	Madeira, Seine Seamount	Phosphorite breccia under a Mn crust	Eocene–Oligocene for the old crust (30–40 Ma) and Upper Miocene–Pliocene for apatite replacing Mn oxides [45]	Early–Middle Miocene: phosphatization on substrate rocks dated at 22.0 ± 0.2 Ma [46]
JC 142-061-016H	IGME-CSIC	Canary Island Seamount Province, Tropic Seamount	Phosphorite serving as substrate for Fe-Mn nodules	~84 Ma for the oldest phosphorite crust, ~38 Ma for a major phosphatization event [22], and widespread phosphatization and Fe–Mn re-nucleation during the early Miocene [47]	38 Ma (age of the major phosphatization event)

The northern zone of interest is the Galicia Bank. Located about 200 km west of Galicia along the northwestern Iberian margin (Figure 1), the Galicia Bank top lies at depths between 700 and 1800 m. Spanning an area of 2117 km^2, it stands out as the dominant structural high in the region, ascending from the surrounding seafloor at depths ranging from 3800 to 620 m. Phosphorites from the Galicia Bank have been previously investigated [20]. The authors reported their occurrence as slabs and nodules that replace limestone while preserving the original protolith fabric. In a subsequent diagenetic phase, these phosphorites were replaced by manganese oxides. Phosphatization is interpreted to have occurred shortly after—or concurrently with—carbonate sedimentation, during two distinct intervals in the late Oligocene and early Miocene, as indicated by strontium isotope

analyses. The radiogenic strontium isotope signatures of the phosphorites (average $^{87}Sr/^{86}Sr$ ratio of 0.713551) suggest the influence of deep-sourced hydrothermal fluids, likely associated with the leaching of granodioritic to granitic basement rocks from the Variscan Iberian Massif underlying the Galicia Bank [20].

The second studied zone is the Madeira-Tore seamount chain, which stretches from the Portuguese mainland to the Madeira archipelago, and more precisely the Seine Seamount. The Seine Seamount, that is almost circular in shape, is located approximately 185 km northeast of Madeira Island. The seamount rises from depths greater than 4000 m to a summit plateau located between 160 and 170 m below sea level [48,49]. The $^{40}Ar/^{39}Ar$ dating of amphibole from basanite forming the substrate at the Seine Seamount yielded an age of 24.4 ± 0.4 Ma, as reported in the study on multi-phase Cretaceous to Quaternary alkaline magmatism on the Tore-Madeira Rise and adjacent seamounts [50]. In contrast, an earlier analysis of the matrix (volcanic) material yielded a younger age of 22.0 ± 0.2 Ma ($^{40}Ar/^{39}Ar$ dating of the groundmass [46]). Phosphorites associated with manganese oxides have been identified along the Madeira-Tore seamount chain, though previous studies have only provided limited insight [45,48,49]. In this region, phosphorites are relatively rare and are thought to have formed at water depths between 1200 and 1500 m [48]. Phosphorites in the Seine Seamount have not been dated. Interestingly, samples from the nearby Lion Seamount—located close to the Seine Seamount—contain a thick, older generation of phosphatized material, dated to approximately 30–40 million years ago based on strontium isotope analysis of apatite [45]. Additionally, apatite has been found impregnating manganese crusts in the area, with the onset of crust formation dated to approximately 8.5 Ma using ^{10}Be isotopic dating [45].

The third area of interest is the Tropic Seamount, the southernmost feature of the Canary Island Seamount Province (Figure 1). It is characterized by a flat summit located at a depth of approximately 1000 m, rising from an abyssal plain at around 4100 m depth [51,52]. The top and flanks of the Tropic Seamount host closely associated phosphorites and Fe-Mn oxyhydroxides, which have been the focus of extensive studies [21–23,45,52–55]. Phosphatization is believed to occur at various stages during the development of Fe-Mn crusts [22,23,47]. Several authors [23] have proposed that this process causes the partial dissolution of pre-existing Mn oxides, a hypothesis that is still under debate [54].

On the Tropic Seamount, a phosphatized, biogenic debris-rich carbonate layer forms the substrate beneath most Fe-Mn crusts. This substrate has an upper age limit of 84 ± 4 million years, based on U-Pb dating [22]. This age is constrained by the age of the volcanic edifice itself (119 Ma) [56] and the earliest known growth of Fe-Mn crusts (73–77 Ma) [21,53]. A major phosphatization event affecting the Fe-Mn core is dated to the Late Eocene (38 ± 1.2 Ma), coinciding with a significant shift in ocean circulation associated with the onset of Antarctic glaciation [22]. Additionally, widespread phosphatization and Fe–Mn re-nucleation are thought to correspond to global phosphogenetic events during the Early Miocene [47].

3. Material and Methods

Two samples provided by the Instituto Geológico y Minero de España (IGME) originated from the Galicia Bank: ARTABRIA II-36DRN and ARTABRIA II-81DRR (DIVA ARTABRIA project). The latter (ARTABRIA II-81DRR) was collected by dredge haul from a station associated with an unconformity forming the southeastern morphological margin of the Galicia Bank, at a water depth between 1540 and 830 m [20]. The former sample (ARTABRIA II-36DRN) was recovered from the eastern slope of the Galicia Bank, dredged at depths ranging from 1555 to 760 m [20]. A third sample, 3521-6, comes from the Seine Seamount, located near Madeira, and is part of the collection of the IPMA (Instituto Português do Mar e da Atmosfera). The samples were collected at 1362 m depth [49]. The fourth sample, JC142-061-016H, provided by the IGME was sampled by ROV-ISIS

(Marine-E Tech project) on the northern flank of the Tropic Seamount, located in the Canary Islands region, at approximately 1100 m depth [55].

Sample characterization involved a combination of imaging, geochemical, and high-resolution isotopic techniques. Surface textures and mineral associations were first examined by scanning electron microscopy (SEM) using a Quanta 200 ESEM (FEI Company, Hillsboro, OR, USA) equipped with an Apollo 10 Silicon Drift EDS detector (EDAX Inc., Mahwah, NJ, USA) at the Institute of Natural Sciences (Brussels). Cathodoluminescence (CL) imaging was performed at UMONS using a Mk5 cold-cathode system (Cambridge Image Technology Ltd., Cambridge, UK), operated at 15 kV and 500 μA, with an electron beam covering a 12 × 4 mm area (~10 μA/mm^2). Laser-induced breakdown spectroscopy (LIBS) is a rapid, spatially resolved, multi-elemental technique, LIBS has emerged as a valuable tool for mineral exploration and trace element mapping, regardless of mineralization [57–59]. It was conducted using a custom-built system at UMONS, comprising a Q-switched Nd:YAG laser (266 nm, 15 mJ, 5 ns pulse duration) and a 9-channel CCD spectrometer (190–1100 nm range, 0.05–0.2 nm resolution). The samples were mounted on a motorized XY stage synchronized with the laser to produce LIBS maps. Ablation craters (~200 μm diameter) corresponded to a fluence of 48 J/cm^2 and an irradiance of 9.5 GW/cm^2. Emission was collected through optical fibers and analyzed with a delay of 1 μs and a 1 ms integration time to minimize background continuum. Laser pulse energy showed a 4.1% relative standard deviation (RSD) after thermal stabilization. Data were processed using spectragryph v1.2 (Dr. Friedrich Menges, Oberstdorf, Germany) and Fiji/ImageJ software (Jython/Java scripting; National Institutes of Health, Bethesda, MD, USA), yielding qualitative hyperspectral LIBS maps for selected elements (e.g., P, CaF, Y, and Li) based on both internal reference spectra and the NIST atomic database. Raman spectroscopy was performed at the Royal Belgian Institute of Natural Sciences to investigate the fluorescence induced by the REEs. We used a 532 nm (green) laser Raman spectrometer (Senterra, Olympus BX51, Bruker Optics GmbH, Ettlingen, Germany). The spectra were acquired using 2 mW excitation power, 5 × 30 s integration time and a 50 μm spectrometer slit. The data were processed using spectragryph v1.2 optical spectroscopy software (Dr. Friedrich Menges, Oberstdorf, Germany). The Raman shift has been transformed into wavelengths according to the following formula: Wavelength (nm) = (Laser wavelength-1 − Raman shift × 10^{-7})$^{-1}$. Here, the laser wavelength was 532 nm and the Raman shift is given in cm^{-1}.

Quantitative major element compositions (Supplementary Material S1—Table S1) were determined via electron microprobe analysis (EMPA) using a JEOL JXA8530F instrument (JEOL Ltd., Tokyo, Japan) at KU Leuven's Department of Materials Engineering. Operating conditions were 15 kV, 10 nA, and a 10 μm beam diameter. Standard minerals used included apatite (F, CaO, P_2O_5), diopside (SiO_2), barite (BaO, SO_3), hematite (FeO), tugtupite (Na_2O, Cl), olivine (MgO), celestite (SrO), and rhodonite (MnO). The Lα line was used for Sr and Ba, and the Kα line was used for the other elements. Detection limits were generally better than 0.05 wt%, with peak counting times of 20 s (40 s for Ba, 80 s for Cl and S).

Trace element concentrations were measured by LA-ICP-MS at the Norwegian Geological Survey (NGU) using a Teledyne-Cetac Analyte Excite 193 nm excimer laser (Teledyne CETAC Technologies, Omaha, NE, USA) coupled to an Agilent 8900 QqQ-ICP-MS (Agilent Technologies, Santa Clara, CA, USA). Ablation was performed under helium with a 50 μm spot size, 10 Hz repetition rate, and 4 J/cm^2 fluence for 45 s. Helium-carried aerosol was mixed with argon before entering the plasma. Calibration used NIST SRM 610 with ^{44}Ca as the internal standard, while NIST SRM 612 and 614 served as quality controls. CaO concentrations in apatite grains, measured by EMPA, ranged from 42.4 to 56.3 wt% due to varying oxide intergrowths. To account for this heterogeneity, average CaO contents per sample were used for internal standardization (e.g., 53.54 wt% for JC142-061, 53.34 wt% for ARTABRIA II-36DRN, 50.43 wt% for ARTABRIA II-81DRR,

46.00 wt% for 3521-6). REE precision was better than 10%. Data were reduced using Iolite [60] with the "trace elements" scheme, and detection limits followed Longerich et al. [61]. Full instrumental settings are detailed in Supplementary Material S2.

Oxygen and strontium isotopes provide critical constraints on the genesis and diagenetic evolution of sedimentary apatite [27,33]. However, such isotopic tools remain largely underutilized in both sedimentary and igneous contexts [62–72].

Oxygen isotope compositions ($\delta^{18}O$) (Supplementary Material S1—Table S2) were analyzed using a Cameca IMS 1270 E7 ion microprobe (SIMS; CAMECA, Gennevilliers, France) at CRPG Nancy. A Cs^+ primary ion beam (3.5 nA) was focused on a 15 μm diameter spot, with charge compensation provided by an electron gun. Secondary negative ions were detected at a mass resolution of 3000 and energy slit of 35 eV. Surfaces were pre-sputtered for 90 s to remove surface contamination. Isotopic measurements were performed in multi-collection mode using Faraday cups, with a total integration time of 150 s and internal precision around 0.1‰. Instrumental mass fractionation was corrected using Durango apatite ($\delta^{18}O$ = 9.4‰ [73]), measured before and after each sample. External reproducibility (2σ) ranged from 0.15 to 0.20‰, and instrumental fractionation of $^{18}O/^{16}O$ varied between 3 and 4‰. Values are reported relative to SMOW, with errors calculated as the quadratic sum of internal and external uncertainties.

Strontium isotopic ratios ($^{87}Sr/^{86}Sr$) in apatite (Supplementary Material S1—Table S3) were measured by LA-MC-ICP-MS at the MiMaC facility (NGU), using a Photon Machines Analyte Excite 193 nm excimer laser (Photon Machines Inc., Bozeman, MT, USA) and a Nu Plasma 3 MC-ICP-MS (Nu Instruments Ltd., Wrexham, UK). Ablation was carried out using a 50 μm spot size, 10 Hz repetition rate, 4 J/cm² fluence, and 30 s duration. Helium was used as a carrier gas, mixed with argon prior to plasma introduction. Ion beams for mass/charge ratios 80, 82–88, and intermediate half-masses (82.5–87.5) were measured in static mode on Faraday cups. Data reduction was performed using Iolite with the "Sr isotopes universal" scheme [74]. Corrections for isobaric interferences from REE++ and Rb were applied. Madagascar apatite served as the primary reference material, while Durango, McClure Mountain, Slyudyanka, and Otter Lake apatite were used to construct a correction curve for CaPO polyatomic interferences. These interferences were minimized during tuning, with a maximum correction factor of 1.00012 for samples and 1.00051 for the lowest Sr reference material (Durango). Full instrumental settings are detailed in Supplementary Material S2.

4. Results

4.1. Macroscopic and Petrographic Description

In this study, two markedly different types of phosphorites from the Galicia Bank were examined. The first type is stratified, featuring multiple phosphate-enriched centimeter to millimeter subparallel beds within a carbonate host rock (Figure 2A). These beds are composed of fine-grained apatite that embeds or replaces micrometric calcite grains (Figure 3A–C). The phosphorite slab is encrusted on its upper surface by an Fe–Mn crust patina and hosts benthic organisms such as cold-water corals. The second type is a compact slab characterized by abundant boring tubes filled by carbonates and consolidated sediments, and highly impregnated with Mn-Fe oxides, specifically 10 Å and 7 Å manganates [20] (Figure 2B). In this variant, apatite also occurs as fine grains and likely represents the phosphatized cement of the original carbonate rock. This cement fills bioclastic components such as foraminifers, coccoliths, and other shell fragments (Figure 3D,E), with minimal calcite remaining.

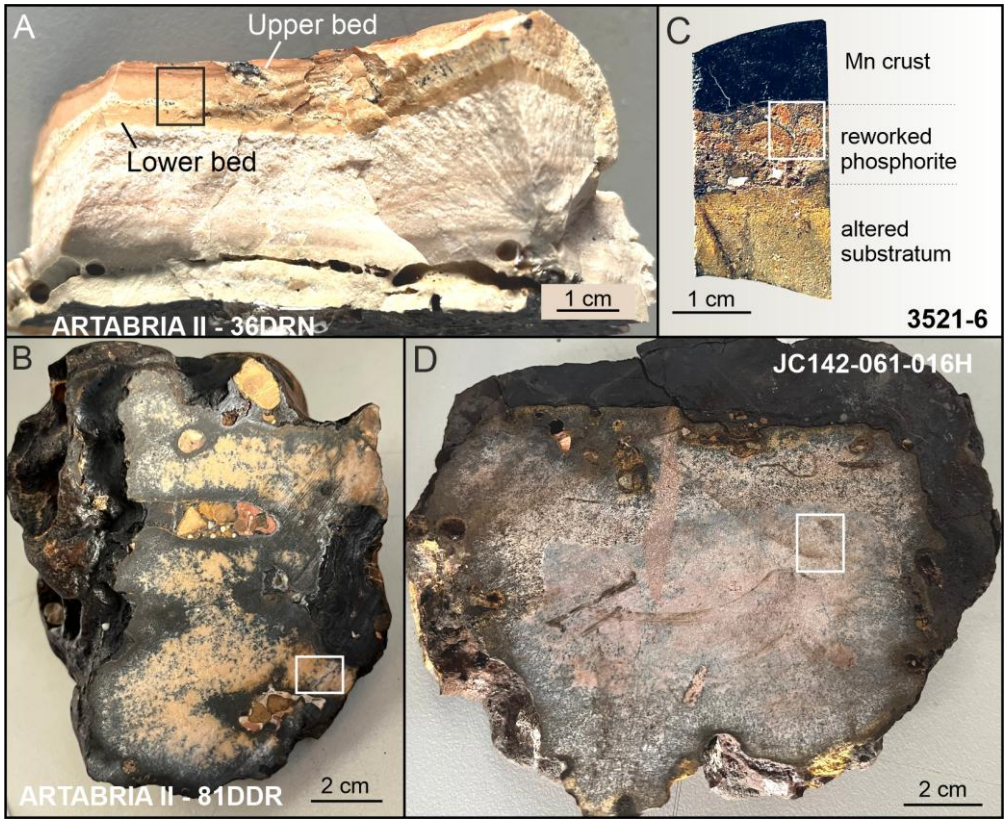

Figure 2. Macrophotographs of the studied phosphorite specimens. (**A**) Layered phosphorite from the Galicia Bank. (**B**) Phosphorite slab impregnated by Mn-Fe oxides from the Galicia bank. (**C**) Reworked phosphorite under a Mn crust from the Seine Seamount (Madeira). (**D**) Phosphorite slab impregnated by Mn-Fe oxides from the Tropic Seamount (Canary Islands). The black (**A**) or white (**B**–**D**) rectangles indicate the areas that were sampled for further SEM, CL, and in situ analyses.

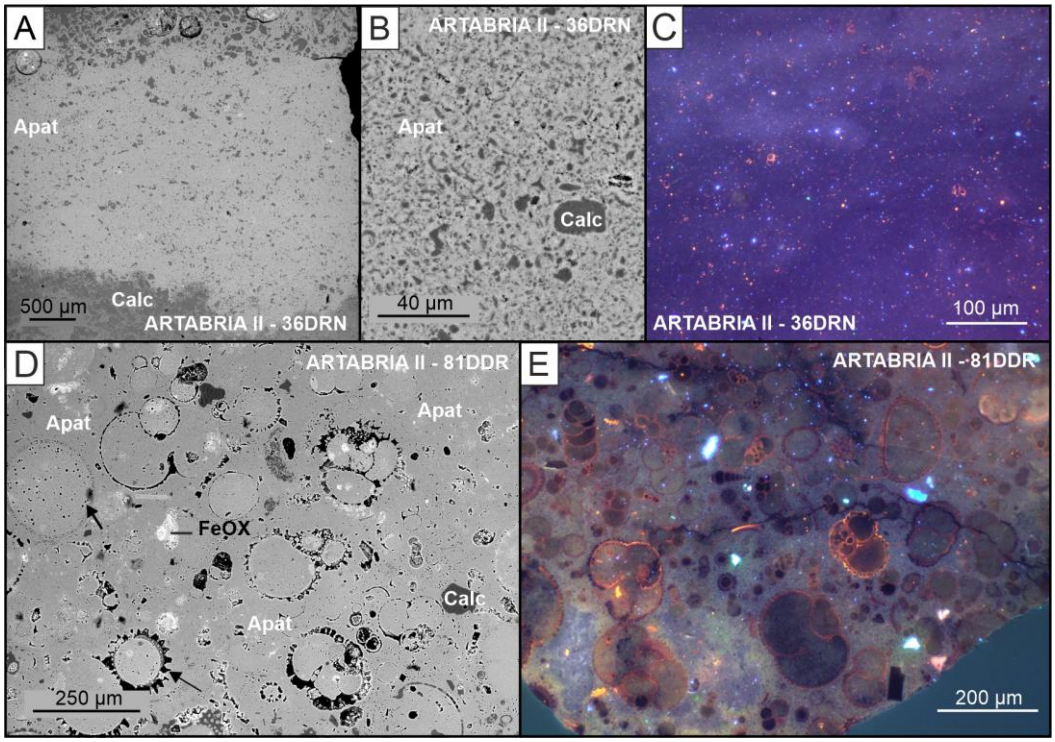

Figure 3. Backscattered electron (**A**,**B**,**D**) and cathodoluminescence (**C**,**E**) micrographs of the phosphorites of the Galicia Bank. The abbreviations used are: Apat for apatite, Calc for calcite, FeOX for Fe oxides. (**A**) Phosphorite bed composed of fine-grained apatite. (**B**) Detailed view of (**A**). (**C**) Violet

to brownish-luminescent phosphatic grains forming the phosphorite bed, including numerous small red-luminescent calcite grains. (**D**) Phosphatized cement in a phosphorite slab that is reworked by Mn-Fe oxides. Bioclasts such as foraminifers (see black arrow), coccoliths and other shells are abundant. However, as emphasized in (**E**), only part of the shells was still made of orange-luminescent calcite. Most of the phosphorite is made of a brown to violet phosphatic cement.

The phosphorite sample from the Tropic Seamount displays a similar slab-like structure impregnated with dendritic Mn-Fe oxyhydroxides, notably vernadite and goethite [21], growing on top (Figure 2D). As with the Galicia Bank specimen, the primary carbonate cement has undergone phosphatization, although calcitic bioclasts are still present (Figure 4A,B) in a higher proportion than in the Galicia Bank.

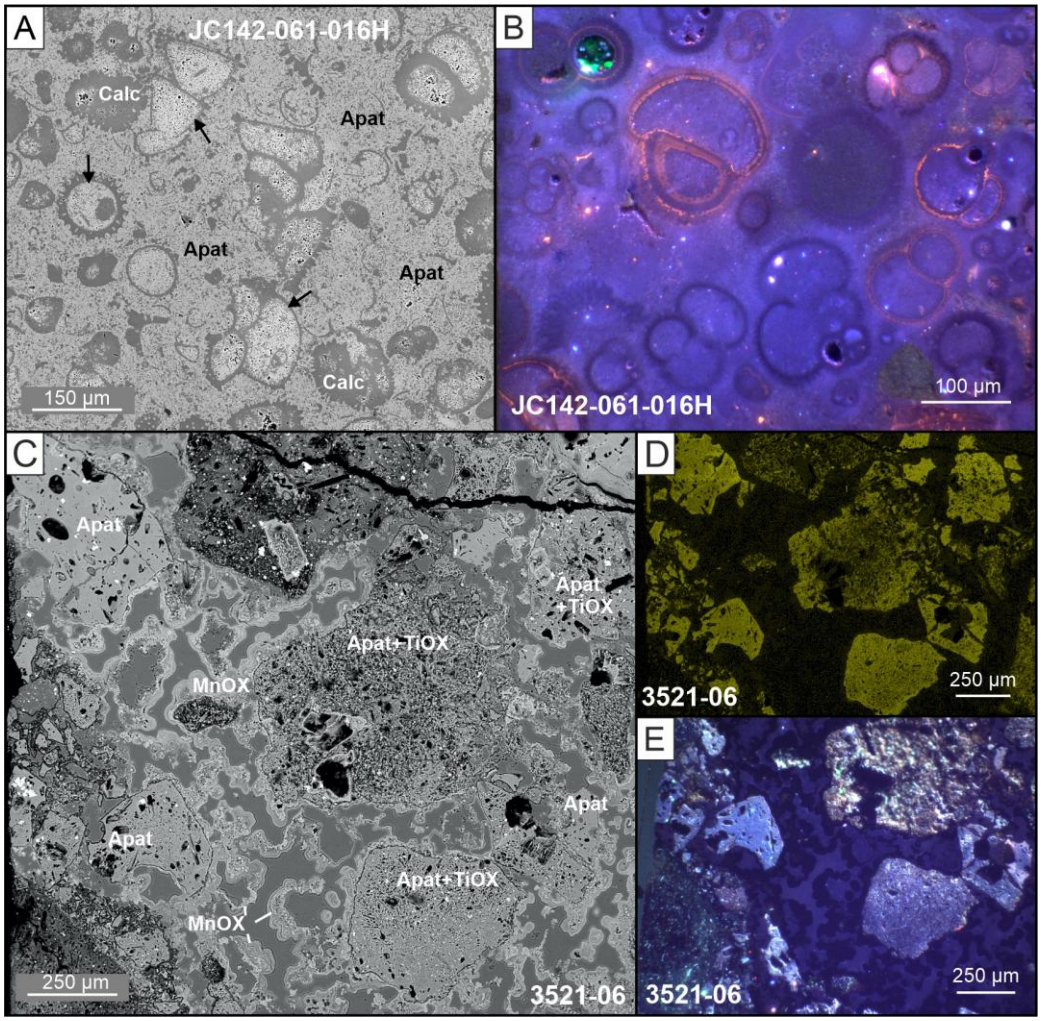

Figure 4. Backscattered electron (**A**,**C**,**D**), and cathodoluminescence (**B**,**E**) micrographs of the phosphorites of the Tropic Seamount (Canary Islands, (**A**,**B**)) and the Seine Seamount (Madeira, (**C**–**E**)). The abbreviations used are Apat for apatite, Calc for calcite, MnOX for Fe oxides, and TiOX for Ti-Fe oxides. (**A**) Phosphatized cement rich in bioclasts. Calcite is still abundant as foraminifers, coccoliths and other shells. The arrows indicate bioclast infillings that are richer in Fe than the surrounding phosphatic cement. (**B**) Violet to brownish-luminescent apatite forming the cement of the phosphorite. Calcite in shells is orange-luminescent. (**C**) Reworked phosphorite that forms a clast-supported breccia. Most of the discontinuities between the phosphorite clasts are underlined by thin Mn oxide concretions. The clasts themselves consist of an intimate mixture of apatite and Ti-Fe oxides, as shown in (**D**), where the EDS elemental map for phosphorus displays varying shades of yellow, brighter yellow indicating higher apatite content, and in (**E**), where the clasts richest in apatite exhibit the strongest blue luminescence.

https://doi.org/10.3390/min16060661

The sample from Seine Seamount differs, consisting of reworked phosphorite overlain by a Fe-Mn crust composed of vernadite (Figure 2C) (as determined in previous studies [48,49]). It forms a clast-supported breccia, with clasts that are generally under one centimeter in size and embedded by localized Mn oxide concretions (Figure 4C). Notably, several of these apatite clasts are actually made of apatite finely intermixed with a Ti-rich Fe oxyhydroxide phase. Figure 4D (EDS map of P) and Figure 4E (CL image) illustrate the variations in the proportions of apatite and Ti-Fe oxide fine mixing, as evidenced by the color differences among the clasts that highlight the extent of mixing. Tiny Mg-rich laths are also observed within brecciated phosphorite.

4.2. Apatite Mineralogy and Chemistry

Apatite from the studied phosphate samples displays a wide range of CaO contents (42.44 wt% in the Ti-rich phosphorite to 56.27 wt% in the most pristine phosphorite clasts) and P_2O_5 concentrations (27.27–33.90 wt%; Supplementary Material Table S1). The lower phosphate contents likely correspond to a deficit at the P site, which can be attributed to the substitution of CO_3^{2-} at this site, as observed in francolite. Apart from one low value (1.79 wt% F), the fluorine content ranges from 3.12 to 5.31 wt%. Chlorine concentrations are generally below the detection limit. SO_3 content is significant in all samples, ranging from 0.83 to 2.33 wt%. SiO_2 concentrations are low to moderate in apatite from the Galicia Bank and the Tropic Seamount (up to 2.26 wt%) but higher in samples from the Seine Seamount (ranging from 0.65 to 4.53 wt%). FeO and Na_2O contents are moderate in most apatites (FeO < 0.81 wt% and Na_2O between 0.46 and 1.04 wt%). However, FeO content reaches 3.90 wt% in the Fe-Mn-mineralized sample from the Galicia Bank and up to 9.49 wt% in the reworked phosphorite from the Seine Seamount. MnO content is low to moderate (<0.91 wt%). Similarly, SrO and MgO contents are low to moderate, reaching up to 0.28 wt% and 0.83 wt%, respectively. BaO content is above the detection limit in only one sample (0.05 wt%) (Supplementary Material Table S1).

4.3. REE and Trace Elements Content

The REE patterns of apatite from the studied phosphorites, normalized to Post-Archean Australian Shale (PAAS [75]), are broadly similar and display flat to HREE-enriched trends, along with pronounced depletion in cerium (Ce) (Figure 5). In situ LA-ICP-MS analyses show that apatite from the Tropic Seamount is notably depleted in REEs compared to PAAS, with total REE concentrations ranging from 5 to 12 ppm. In contrast, apatite from the layered phosphorite at the Galicia Bank exhibits two distinct REE content ranges depending on the stratigraphic bed: ΣREE = 122–177 ppm in the lower bed and ΣREE = 843–1098 ppm in the upper bed. The upper bed also shows a slight enrichment in MREEs relative to the lower bed. Apatite from the Fe-Mn mineralized slab at the Galicia Bank displays REE concentrations similar to those of the upper bed (ΣREE = 411–1138 ppm; Table 2). The highest REE contents are found in apatite from the Seine Seamount, with concentrations ranging from 1671 to 3226 ppm. Apatite from the Seine Seamount, finely intermixed with a Ti-rich Fe oxyhydroxide phase, shows significantly enriched in Ti (up to 1.6 wt%) and Fe (up to 11.6 wt%; Table 2). The relative REE enrichment in apatite—highest in the Seine Seamount phosphorite, followed by the reworked phosphorite from the Galicia Bank, the lower bed of the layered phosphorite from the same site, and finally the Tropic Seamount phosphorite—is also reflected in the Raman spectroscopy data. Specifically, the relative intensity of the Nd-induced fluorescence emission peak varies consistently with this trend (Figure 6).

Table 2. Selected LA-ICPMS analyses (in ppm) of apatite (normalization to Post-Archean Australian Shale [75]).

			ppm																				
Locality	**Sample**	**Analysis Spot**	**La**	**Ce**	**Pr**	**Nd**	**Sm**	**Eu**	**Gd**	**Tb**	**Dy**	**Ho**	**Er**	**Tm**	**Yb**	**Lu**	**Y**	**Th**	**Ti**	**Fe**	**ΣREE**	**(La/Yb)$_N$**	**Ce/Ce ***
Tropic Seamount	JC142-061-016H	JC142-061-016H-1	3	1.0	0.3	1.1	0.2	0.0	0.2	0.0	0.3	0.1	0.2	0.0	0.4	0.1	4	0.1	64	3014	6	0.6	0.23
		JC142-061-016H-3	4	1.6	0.6	2.1	0.4	0.1	0.5	0.1	0.5	0.1	0.4	0.1	0.5	0.1	6	0.2	25	1091	10	0.6	0.25
		JC142-061-016H-4	3	1.3	0.5	2.0	0.4	0.1	0.5	0.1	0.5	0.1	0.3	0.1	0.4	0.1	5	0.1	23	1063	9	0.6	0.23
		JC142-061-016H-5	3	1.2	0.4	1.5	0.3	0.1	0.4	0.0	0.4	0.1	0.3	0.1	0.4	0.1	4	0.1	16	778	8	0.5	0.24
		JC142-061-016H-6	2	0.9	0.3	1.2	0.2	0.0	0.3	0.0	0.3	0.0	0.2	0.0	0.3	0.0	3	0.1	19	1431	6	0.5	0.24
		JC142-061-016H-7	2	1.0	0.3	1.1	0.2	0.0	0.3	0.0	0.3	0.0	0.2	0.0	0.3	0.0	3	0.1	14	568	6	0.5	0.27
		JC142-061-016H-8	4	1.6	0.5	2.2	0.4	0.1	0.5	0.1	0.5	0.1	0.4	0.1	0.5	0.1	6	0.1	25	855	10	0.6	0.24
		JC142-061-016H-9	2	0.8	0.3	1.0	0.2	0.0	0.2	0.0	0.3	0.0	0.2	0.0	0.3	0.0	3	0.0	28	1022	5	0.5	0.26
		JC142-061-016H-10	3	1.6	0.5	2.2	0.4	0.1	0.5	0.1	0.5	0.1	0.3	0.1	0.4	0.1	5	0.1	28	735	10	0.6	0.27
		JC142-061-016H-11	4	1.9	0.6	2.4	0.5	0.1	0.6	0.1	0.6	0.1	0.4	0.1	0.5	0.1	7	0.2	46	1543	12	0.6	0.26
		JC142-061-016H-12	4	1.7	0.6	2.2	0.5	0.1	0.6	0.1	0.6	0.1	0.4	0.1	0.5	0.1	6	0.2	35	1212	11	0.6	0.25
		JC142-061-016H-13	3	1.5	0.4	1.8	0.3	0.1	0.4	0.0	0.4	0.1	0.3	0.1	0.4	0.1	5	0.1	26	796	9	0.6	0.26
		JC142-061-016H-14	3	1.3	0.4	1.5	0.3	0.0	0.3	0.0	0.4	0.1	0.3	0.1	0.4	0.1	4	0.1	37	1165	8	0.6	0.26
Galicia Bank	ARTABRIAII-36DRN (Upper bed)	ArtabriaII-36DRN-1	402	20.1	70	300	61	16.7	77.8	11.2	72.1	17.2	51.5	6.6	39.2	6.3	747	1.0	201	2867	1081	0.8	0.03
		ArtabriaII-36DRN-2	405	20.3	70	306	61	16.8	78.4	11.4	75.0	18.1	53.6	6.9	41.0	6.7	775	0.7	227	2920	1098	0.7	0.03
		ArtabriaII-36DRN-3	358	17.7	64	262	51	14.3	66.5	9.7	64.1	15.4	45.7	6.0	36.3	5.9	670	0.5	185	2471	954	0.7	0.03
		ArtabriaII-36DRN-4	355	16.5	61	249	48	13.4	63.7	9.3	62.1	15.0	45.4	6.0	36.1	5.9	678	0.7	309	2717	925	0.7	0.03
		ArtabriaII-36DRN-5	337	16.2	55	219	41	11.4	54.7	8.0	54.8	13.8	42.8	5.7	34.5	5.8	641	0.8	235	2822	843	0.7	0.03
		ArtabriaII-36DRN-23	390	20.4	70	298	59	16.3	76.0	10.9	72.2	17.6	51.6	6.7	40.0	6.5	764	0.7	186	2662	1065	0.7	0.03
		ArtabriaII-36DRN-24	388	18.8	67	291	59	16.0	75.7	10.8	71.0	17.0	50.3	6.5	38.8	6.3	728	0.7	259	2750	1046	0.7	0.03
		ArtabriaII-36DRN-25	375	18.6	66	269	52	14.3	67.6	9.8	64.9	16.2	48.1	6.3	37.8	6.1	704	0.5	167	2657	987	0.7	0.03
	ARTABRIAII-36DRN (Lower bed)	ArtabriaII-36DRN-8	94	10.6	7	26	4	1.1	6.9	1.1	9.2	3.0	10.9	1.7	11.8	2.1	199	0.6	191	2923	177	0.6	0.08
		ArtabriaII-36DRN-10	81	4.1	7	25	4	1.2	6.9	1.0	7.6	2.2	7.6	1.1	7.2	1.3	139	0.4	73	2134	148	0.8	0.04
		ArtabriaII-36DRN-11	84	3.6	7	27	4	1.2	7.3	1.1	8.1	2.3	8.0	1.1	7.6	1.4	146	0.3	90	2810	154	0.8	0.03
		ArtabriaII-36DRN-12	80	3.6	6	25	4	1.1	6.5	1.0	7.5	2.2	7.2	1.0	7.0	1.3	134	0.3	79	1795	144	0.8	0.03
		ArtabriaII-36DRN-13	81	3.6	6	24	4	1.1	6.6	1.0	7.4	2.1	7.2	1.0	6.8	1.2	132	0.3	78	2051	143	0.9	0.03
		ArtabriaII-36DRN-14	70	3.1	5	21	3	0.9	5.6	0.8	6.3	1.8	6.1	0.9	5.5	1.0	111	0.3	67	1478	124	0.9	0.03
		ArtabriaII-36DRN-15	70	2.9	5	20	3	1.0	5.4	0.8	6.2	1.7	5.9	0.8	5.4	1.0	110	0.3	74	1353	122	1.0	0.03
	ARTABRIAII-81DRR	ArtabriaII-81DDR-1	352	17.5	61	253	49	13.5	63.4	9.2	60.8	15.2	45.1	5.9	35.5	5.8	660	0.5	156	2492	949	0.7	0.03
		ArtabriaII-81DDR-2	335	65.6	52	211	41	11.5	56.0	8.2	57.0	14.6	46.8	6.3	37.5	6.4	665	2.5	674	56,093	650	0.7	0.11
		ArtabriaII-81DDR-3	244	44.5	34	133	23	7.0	35.1	5.4	38.7	10.6	33.9	4.8	30.2	5.2	468	0.7	109	14,578	757	0.6	0.11
		ArtabriaII-81DDR-4	269	60.6	40	158	31	8.7	43.7	6.6	46.9	12.1	38.0	5.3	32.6	5.3	530	1.2	167	14,292	411	0.6	0.13
		ArtabriaII-81DDR-5	172	19.2	19	78	14	3.9	21.6	3.2	24.1	6.6	22.1	3.0	19.5	3.5	338	0.8	325	44,418	573	0.7	0.07
		ArtabriaII-81DDR-6	217	43.3	28	112	21	6.0	31.1	4.6	34.6	9.2	31.0	4.3	27.4	4.8	427	0.9	154	26,755	610	0.6	0.12
		ArtabriaII-81DDR-7	222	51.5	31	122	23	6.7	34.0	5.2	36.6	9.7	31.0	4.4	28.1	4.9	449	0.6	228	2299	681	0.6	0.14
		ArtabriaII-81DDR-8	237	71.8	35	142	26	7.4	37.7	5.4	38.9	10.3	31.8	4.5	28.2	4.8	460	2.0	321	3023	552	0.6	0.18
		ArtabriaII-81DDR-9	211	50.6	27	104	19	5.5	28.6	4.3	32.0	8.6	27.7	3.8	25.8	4.4	405	0.7	327	4233	576	0.6	0.15

https://doi.org/10.3390/min16060661

		ArtabriaII-81DDR-10	204	64.4	30	115	22	6.3	31.2	4.5	32.4	8.3	26.7	3.8	24.0	4.3	405	0.7	178	2171	1132	0.6	0.19
		ArtabriaII-81DDR-11	351	102.4	69	282	56	14.9	69.1	10.1	65.8	15.5	46.4	6.1	37.6	6.2	610	4.9	75	7340	721	0.7	0.15
		ArtabriaII-81DDR-12	250	67.2	38	149	29	8.1	43.0	6.3	44.2	11.3	35.0	4.7	30.0	5.1	520	0.9	220	2044	492	0.6	0.16
		ArtabriaII-81DDR-13	187	33.3	25	97	18	5.2	27.5	4.1	30.3	8.1	26.1	3.6	23.0	3.9	380	0.4	73	13,872	447	0.6	0.11
		ArtabriaII-81DDR-14	183	19.8	22	87	15	4.5	24.1	3.7	27.2	7.3	23.8	3.4	22.2	3.8	352	0.5	117	17,930	726	0.6	0.07
		ArtabriaII-81DDR-15	275	43.9	38	149	28	8.1	41.6	6.3	45.0	11.5	36.7	5.1	32.7	5.5	543	0.6	178	26,431	725	0.6	0.10
		ArtabriaII-81DDR-16	267	45.9	38	154	28	8.2	42.3	6.3	45.1	11.7	36.7	5.0	31.7	5.4	512	0.7	148	14,045	378	0.6	0.10
		ArtabriaII-81DDR-19	197	19.8	14	52	7	2.2	13.9	2.1	17.6	5.8	20.3	3.0	20.0	3.6	363	1.3	231	34,016	316	0.7	0.10
		ArtabriaII-81DDR-21	161	14.0	12	46	7	2.1	13.0	2.0	15.5	4.7	16.8	2.5	16.5	2.8	289	1.1	55	15,935	1138	0.8	0.04
		ArtabriaII-81DDR-22	475	24.9	60	248	42	11.8	63.7	9.6	68.4	18.3	55.8	7.4	45.7	7.6	777	0.3	53	7838	1007	0.8	0.03
		ArtabriaII-81DDR-23	426	19.7	55	213	34	9.9	55.4	8.4	62.1	16.4	50.1	6.9	42.7	7.3	709	0.4	58	5409	883	0.7	0.03
		ArtabriaII-81DDR-24	378	21.4	47	187	31	9.1	49.1	7.2	50.9	13.3	42.0	5.8	35.3	5.8	619	0.6	168	23,443	469	0.8	0.04
		ArtabriaII-81DDR-25	210	8.8	25	94	15	4.4	24.9	3.8	27.5	7.2	23.0	3.2	20.2	3.3	335	0.4	41	6385	1087	0.8	0.03
		ArtabriaII-81DDR-26	428	40.3	61	253	45	12.6	64.5	9.4	62.2	15.1	46.0	6.0	37.1	5.8	675	0.2	133	61,790	877	0.9	0.06
Seine Seamount (Madeira)	3521-6	3521-6	821	291.2	172	559	107	35.8	107.6	16.3	100.2	22.4	64.4	8.5	51.8	8.4	769	18.0	8115	52,722	2572	1.2	0.18
		3521-7	795	238.4	158	503	95	31.4	92.5	13.7	81.7	17.8	52.9	7.2	43.2	6.8	614	17.4	7723	49,661	2323	1.4	0.15
		3521-8	871	317.0	206	693	138	44.2	135.6	20.1	129.0	28.6	83.1	10.8	65.7	10.5	975	17.1	9075	66,383	2992	1.0	0.17
		3521-13	938	291.3	187	711	159	47.9	184.6	28.1	173.4	39.0	105.9	13.4	77.7	12.0	1227	35.3	9804	99,695	3226	0.9	0.16
		3521-16	747	290.6	127	539	99	30.5	110.6	16.4	104.8	23.8	68.1	8.7	52.4	8.2	795	15.9	15,026	115,789	2419	1.1	0.22
		3521-11	666	328.0	119	399	73	24.2	72.4	10.3	64.4	13.8	38.3	5.0	29.7	4.7	465	16.2	11,933	84,985	2009	1.7	0.27
		3521-12	603	257.3	107	387	66	21.6	66.4	9.7	59.1	13.5	39.1	5.0	29.4	4.7	462	13.2	11,924	80,190	1814	1.5	0.23
		3521-14	644	242.6	112	407	84	26.5	97.2	14.7	94.1	21.5	59.6	8.1	45.2	7.1	693	16.7	9443	58,392	2026	1.1	0.21
		3521-15	672	243.4	116	459	88	26.6	100.6	15.2	97.5	22.9	63.9	8.4	48.1	7.6	715	13.9	13,087	79,436	2140	1.0	0.20
		3521-17	486	314.1	89	332	61	18.8	67.7	9.8	62.1	14.4	41.3	5.3	31.5	4.9	503	12.2	15,581	91,275	1671	1.1	0.35

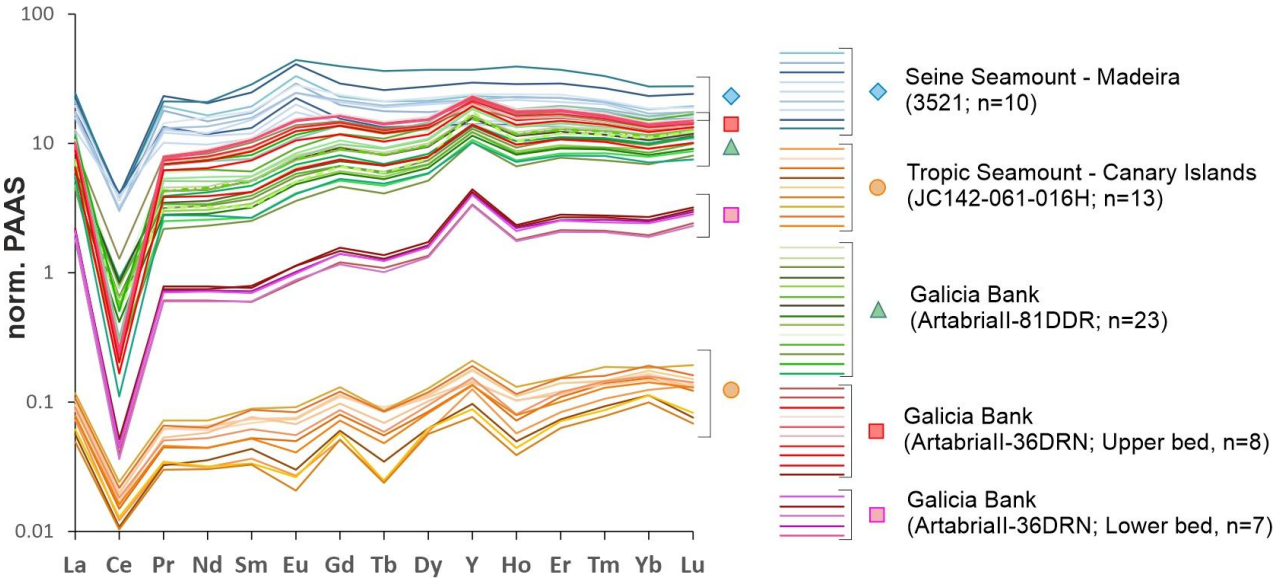

Figure 5. REE patterns of apatite in different investigated phosphorites (LA-ICPMS analyses). REE patterns are normalized to Post-Archean Australian Shale (PAAS [75]).

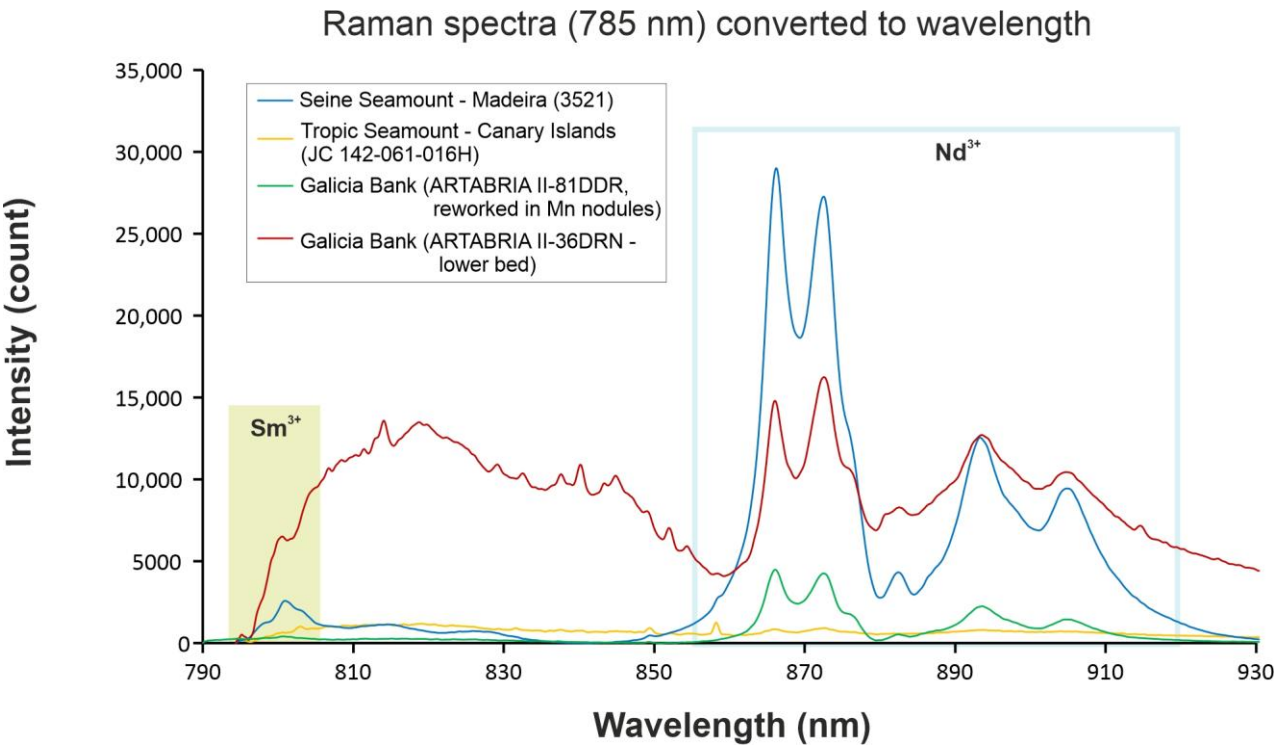

Figure 6. Representative Raman spectra of apatite converted to wavelength of the deep-sea phosphorites. These spectra highlight the relative enrichment in REEs of the phosphorites.

The intensity of Ce anomalies varies among the study sites. The strongest negative Ce anomalies are observed in the Galicia Bank samples, ranging from 0.03 to 0.08 in the layered phosphorites and from 0.03 to 0.19 in the Fe-Mn impregnated reworked slab. In comparison, Ce anomalies in the Seine and Tropic Seamount phosphorites are less pronounced, ranging from 0.15 to 0.35 and 0.23 to 0.27, respectively.

LIBS imaging of the layered phosphorite from the Galicia Bank (Figure 7) reveals the spatial distribution and relative enrichment of several CRM, including P, Y (as a proxy for REEs), F, and Li. The color intensity indicates that the upper bed is more enriched in Li

and Y than the lower bed, in positive correlation with REEs, a pattern corroborated by LA-ICP-MS data (Figure 7).

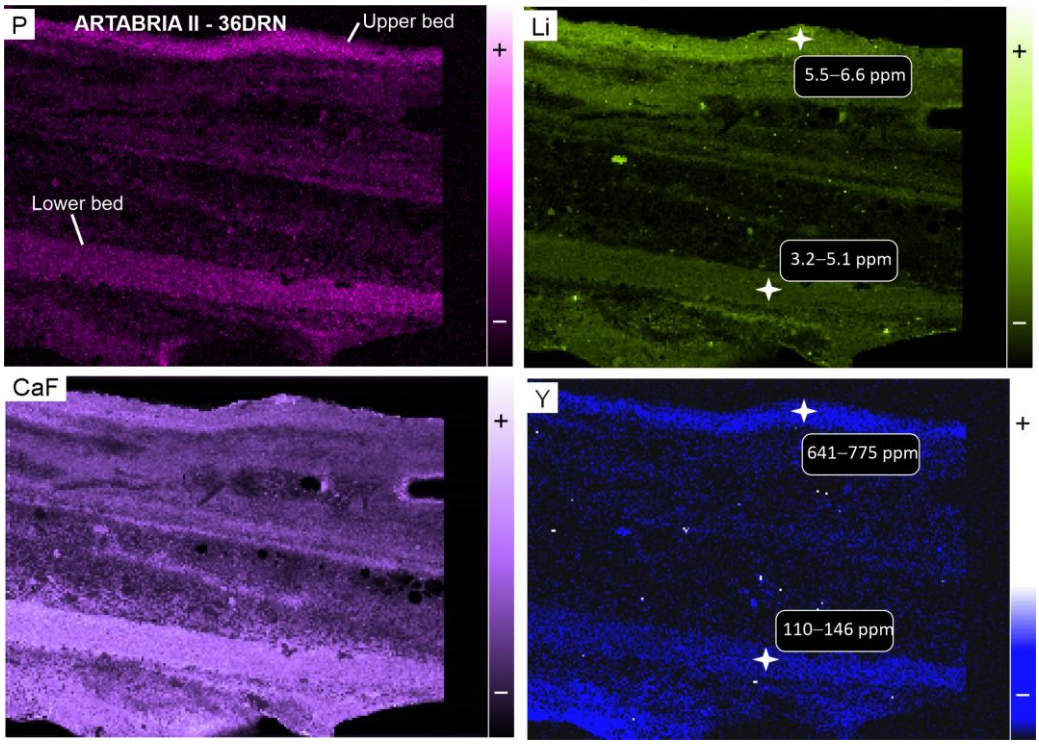

Figure 7. Selected LIBS maps (P, Li, CaF, and Y) of the layered phosphorite from the Galicia Bank (sample 36DNR). Lithium and yttrium La-ICPMS analyses are reported.

4.4. Isotope Data

The oxygen (O) and strontium (Sr) isotopic compositions of apatite are illustrated in Figure 8. The $\delta^{18}O$ values show variability not only between different samples within the same geological zone but also within individual samples. In the reworked phosphorite from the Seine Seamount (sample 3521-6), two distinct ranges of $\delta^{18}O$ values are observed: 18.4–21.5‰ in regions where apatite is dominant and 11.5–17.6‰ where apatite is finely intermingled with Ti-rich Fe oxyhydroxides. It is noticeable that in these regions the apatite itself is highly Fe-enriched, with FeO content up to 9.49 wt% and CaO content down to 42.44 wt%. Given the cryptocrystalline character of sedimentary carbonate fluorapatite and the close spatial association with Fe–Mn mineralization, part of the measured Fe may originate from finely disseminated Fe oxyhydroxides, submicrometric inclusions or mixed phosphatic–Fe assemblages rather than direct structural incorporation into the apatite lattice. In the absence of any Fe-rich apatite reference material, we cannot quantify the matrix effect associated with this chemical composition change and keep out of the discussion the $\delta^{18}O$ values measured on these Fe rich apatite. For the layered phosphorite from the Galicia Bank (sample ARTABRIA II-36DRN), $\delta^{18}O$ values differ between beds: the upper bed ranges from 21.3 to 21.9‰, while the lower bed exhibits values between 19.0 and 20.2‰. In the Fe-Mn mineralized slab (sample ARTABRIA II-81DRR), apatite displays $\delta^{18}O$ values that are similar to or slightly lower than those of the upper bed of the layered phosphorite, falling within 20.4–21.9‰. Apatite from the Tropic Seamount (sample JC142-061-016H) shows $\delta^{18}O$ values ranging from 19.7 to 22.5‰.

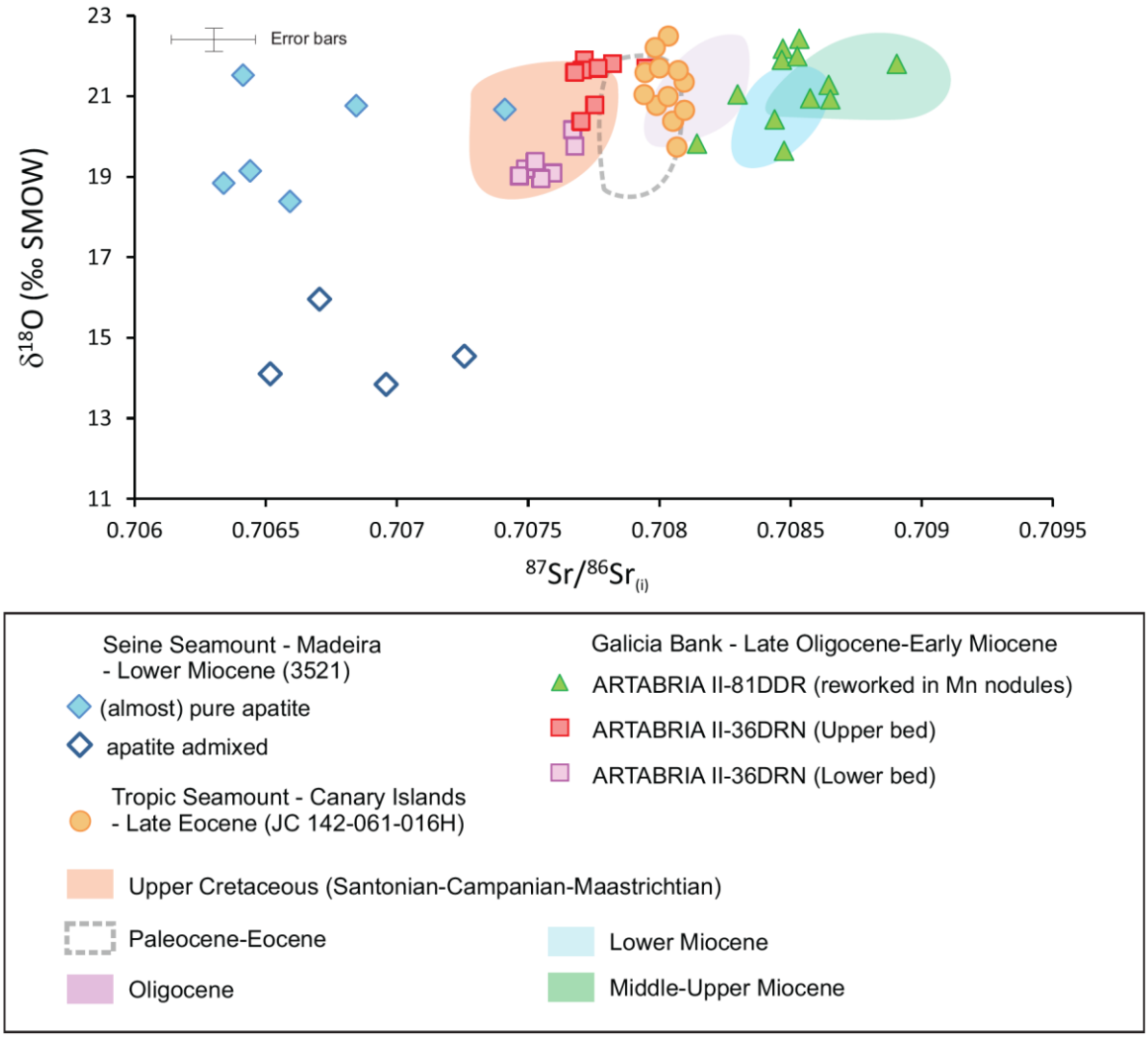

Figure 8. Correlation between in situ $^{87}Sr/^{86}Sr_{(i)}$ (LA-ICPMS analyses) and $\delta^{18}O$ (SIMS analyses) for apatite from phosphorites of the Galicia bank, Seine Seamount and Tropic Seamount. The fields given for comparison represent $d^{18}O$ data on marine phosphatic material (phosphorites, marine fossils, fish teeth, etc.) correlated with seawater Sr isotopic signature of the same age. The represented fields are the Upper Cretaceous [71,76,77], Paleocene–Eocene [71,78–81], Oligocene [71,78,80], Lower Miocene [78,82] and Middle–Upper Miocene [71,78,80,83] Further discussion of the complexity and ages of phosphatization events across the different study sites is provided in the text.

The initial $^{87}Sr/^{86}Sr$ ratios Sr(i) of apatite were calculated based on the most probable age of formation (see Table S3 in the Supplementary Material S1). Similar to oxygen isotopes, Sr(i) values vary within single formations and even within individual samples. In the Seine Seamount phosphorite (3521-06), Sr(i) ranges from 0.7061 to 0.7068 for nearly pure apatite and from 0.7065 to 0.7085 when apatite is intimately mixed with Ti-Fe oxides. In the layered phosphorite from the Galicia Bank (ARTABRIA II-36DRN), Sr(i) varies by bed: apatite in the lower bed is less radiogenic, with values between 0.7074 and 0.7077, while the upper bed ranges from 0.7076 to 0.7079. The Mn-Fe mineralized slab (ARTABRIA II-81DRR) shows higher radiogenic Sr(i) values, ranging from 0.7081 to 0.7089. Finally, apatite from the Tropic Seamount (JC142-061-016H) has initial $^{87}Sr/^{86}Sr$ ratios between 0.7079 and 0.7082.

5. Discussion

5.1. Genesis of the Phosphorites Based on REY

Three phosphorite types are identified: (i) stratified or massive phosphatized carbonates from the Galicia Bank, the latter being impregnated by Fe-Mn oxyhydroxides; (ii) slab-like phosphorites from the Tropic Seamount, also with Fe-Mn oxyhydroxide impregnations; and (iii) reworked brecciated phosphorites from the Seine Seamount, often associated with Fe-Ti phases, reflecting variable degrees of phosphatization and brecciation.

The composition of apatite is highly variable, marked by substitutions (notably CO_3^{2-}), local enrichments in Fe and Si, and significant F and SO_3 contents, reflecting contrasting formation and alteration conditions. The observed Ca^{2+} deficit in apatite may be related to elements that were not analyzed or more likely to coupled substitutions within the apatite structure that generate vacancies at the Ca^{2+} site [84] (Supplementary Material Table S1).

The shape of the REE patterns in apatite from the studied phosphorites is typical of those observed in sedimentary phosphorites, which often reflect the geochemical signature of open-ocean cold seawater [6,28,85,86]. These similarities are even more pronounced when compared to the REE signature of porewaters at the sediment–bottom water interface, which are believed to develop under suboxic conditions [29]. This supports the hypothesis that phosphate mineralization is primarily a post-oxic process occurring under fluctuating redox conditions, as proposed by Jarvis [39]. The influence of oxygenated seawater on sediments where apatite formed is evidenced by the consistent presence of a negative Ce anomaly. This strong negative Ce and positive Y and Gd anomalies (Figure 5) support the derivation of REEs, Y and phosphates from seawater. The magnitude of the Ce anomaly depletion varies, indicating differences in oxidation conditions across the studied sites and even within a single site. The pronounced negative Ce anomalies recorded in apatite mainly reflect inheritance of the oxidized seawater REE signature existing prior to phosphogenesis, rather than direct Ce fractionation during apatite precipitation [85,87]. Consequently, apatite first preserves a seawater-derived REE fingerprint acquired during phosphogenesis. Nevertheless, significant variations occur between Galicia Bank, Tropic and Seine Seamount phosphorites. This indicates that Ce behavior was influenced by temporal changes in seawater composition, regional oceanographic settings and local redox conditions. Subsequent interactions with porewaters and post-depositional processes related to Fe–Mn mineralization may also have contributed to partial modification or redistribution of the original REE signal, of which the Ce is an anomaly.

The two apatite-rich layers within the layered phosphorites of the Galicia Bank display distinct REE enrichments, suggesting slight differences in fluid composition or conditions during phosphogenesis. The lower bed shows evidence of a hydrogenous (directly derived from seawater) REE source, with Y/Ho ratios around 60 (Figure 9A,B), close to the seawater signature (Figure 9A–C) [88]. In contrast, the upper bed reflects the influence of a "third" component (likely chemically modified porewater; Figure 9A; [29]). This "third" component is interpreted as a non-detrital source, based on several geochemical features, including low Th contents, Y/Ho ratios exceeding those typical of siliciclastic detrital material (~25–30 [88]), and high ΣREE/Th values. Such characteristics suggest relative enrichment in REE compared to Th during diagenetic redistribution processes [29]. Nonetheless, it is unlikely to be purely hydrogenous due to its relatively lower Y/Ho ratio (~40; Figure 9A,B) compared to seawater (at ~60 [88]) and higher middle REE (MREE) enrichment, as indicated by Sm/Yb ratios (Figure 9B). These REEs may have originated from porewaters influenced by a mix of Fe-Mn oxyhydroxides and phosphate (and possibly a detrital contribution), a hypothesis supported by the overlap between the Mn-Fe concretion field and the primary REE component (Figure 9A).

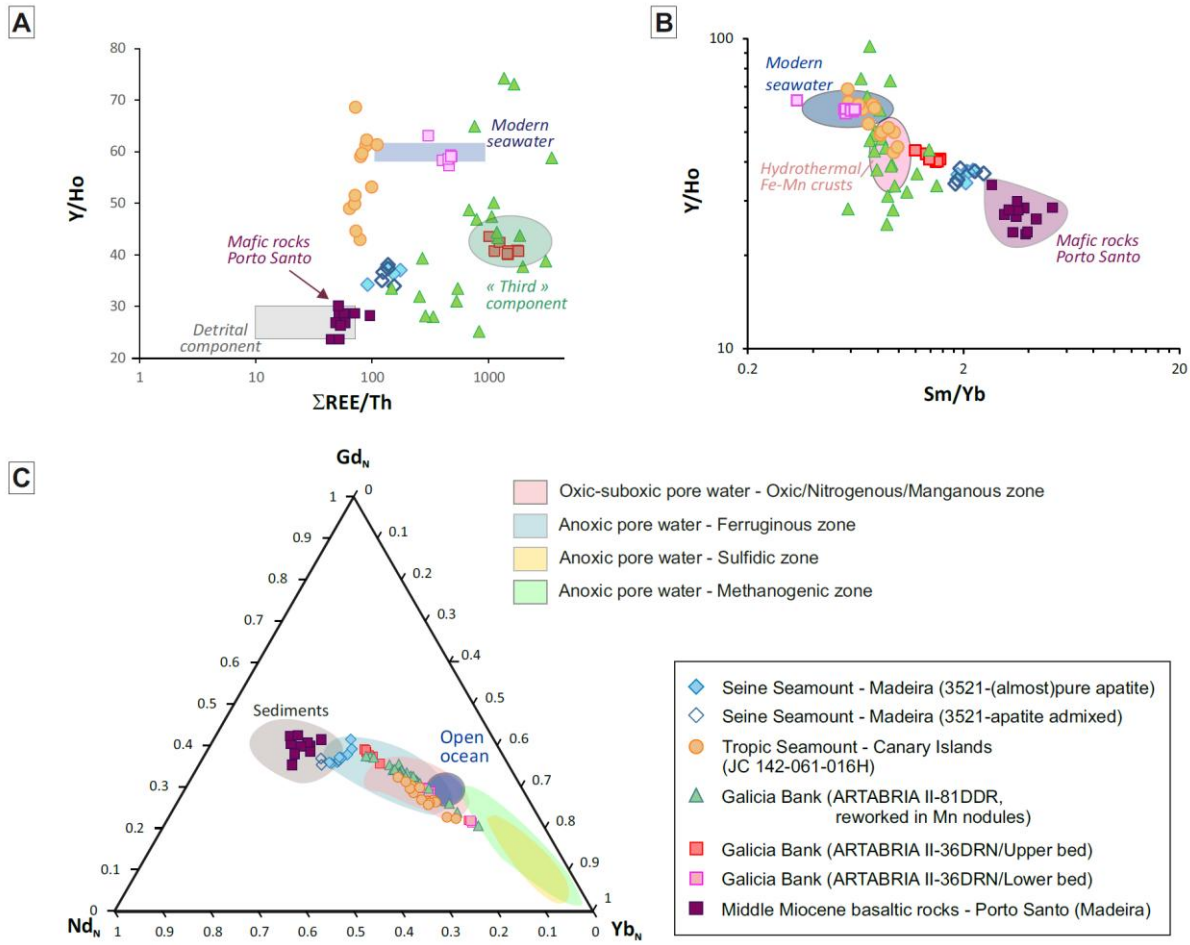

Figure 9. Discrimination diagrams based on LA-ICPMS analyses of the investigated phosphorites. (**A**) Y/Ho vs. ΣREE/Th ratios (modern seawater and detrital components [88]). (**B**) Y/Ho vs. Sm/Y ratios (modern seawater and hydrothermal Fe-Mn crusts after [89]). (**C**) Nd_N–Gd_N–Yb_N ternary diagram of REE signatures (normalised to the North American shale composite [90]). The fields represented are: oxic–suboxic and anoxic pore water [91] as well as sulfidic and methanogenic zones [92]. The data of the Porto Santo basaltic rocks [93] are presented for comparison.

Apatite from the Tropic Seamount phosphorite plots along a trend in the binary and ternary diagrams of Figure 9, with one end-member resembling seawater and the other aligning with phosphorites altered by Mn–Fe oxides. This could suggest that the phosphorite was modified, at least partially, by secondary impregnation. Alternatively, this signature may reflect the presence of pre-existing Fe–Mn oxides in parts of the phosphorite, which subsequently left a geochemical imprint.

A remaining question regarding the Tropic Seamount phosphorite concerns the timing and succession of phosphatization events relative to Fe–Mn crust formation. Previous studies on Mn–Fe oxides and phosphorites [21,22,55] indicate a succession of phosphatization and Fe–Mn precipitation events from the Mesozoic to the present. Therefore, the sample investigated here likely represents only one stage within this multi-phase mineralization history at the Tropic Seamount.

In contrast to the other phosphorites, apatite from the Seine Seamount plots close to the detrital/sedimentary field (Figure 9A,C) and the compositional field of the mafic rocks from Porto Santo. Further discussion is provided in the following section. Overall, the phosphorites studied show evidence of a mixed influence from hydrogenous, detrital, and "third" component sources.

5.2. Further Insights into Element Sources and Age Discussion Based on O and Sr Isotopes

The oxygen and strontium isotopic compositions of ancient apatite are generally considered reliable proxies for the isotopic composition of seawater at the time of phosphogenesis [27,80,94–96]. Post-depositional modifications of apatite—such as diagenesis, weathering, or interaction with hydrothermal fluids—can often be identified by deviations from the expected seawater isotopic signatures of the corresponding age [27,33–35,97]. Oxygen isotopes are especially sensitive to temperature-dependent exchange processes and fluid circulation, whereas Sr isotopes may reflect interaction with porewaters, externally derived fluids, or basement-related inputs. Therefore, part of the isotopic variability observed in the phosphorites may result from post-depositional overprinting processes, including diagenesis, weathering and/or hydrothermal alteration, rather than solely recording primary seawater compositions. At the Tropic Seamount, phosphatization is inferred to have occurred as early as the Upper Cretaceous for the oldest phosphorite crusts (phosphatization of previous carbonates), with a major event during the Early Eocene and another episode in the Early Miocene [22,47]. Sr isotopic data overlap with the isotopic range of Paleocene–Eocene seawater (Figure 8). Additionally, much of the oxygen isotope data fall within the range expected for seawater at the time of phosphogenesis. One might suggest that the shift in Sr isotope composition is due to partial modification of the phosphorite by Mn-Fe oxide impregnation (as proposed in Section 5.1). However, all analyses—even those preserving a seawater-like signature (Figure 9A–C)—fall within the isotopic range of Palaeocene–Eocene seawater. These findings suggest that these phosphorites most likely formed during the major phosphogenic episode around 38 Ma, as previously proposed [22]. Alternatively, the transition from warm to cold circum-Antarctic circulation during the Eocene [22] may have overprinted an earlier phosphorite generation (possibly Cretaceous in age) at the Tropic Seamount during subsequent diagenetic processes. Whichever hypothesis is favored, it is important to emphasize that this finding, which is based on a limited number of samples, does not preclude the occurrence of multiple phosphatization events spanning a wide time interval, from the Cretaceous—potentially related to Tethyan margins and oceanic gateways—to the Miocene, associated with intensified upwelling on Atlantic seamounts. Evidence from the Tropic Seamount illustrates the polyphase nature of phosphogenesis, as textural overprinting and replacement relationships with Fe–Mn crusts, stratigraphic discontinuities, and distinct geochemical signatures reflecting successive episodes of formation controlled by evolving redox conditions and oceanographic changes [21,22,45,53,55,98].

For the Galicia Bank, the Sr isotope composition of the layered phosphorite (sample 36DRN) is less radiogenic than that of Late Oligocene–Early Miocene seawater and instead closely resembles the composition of Upper Cretaceous seawater. This observation appears inconsistent with the hypothesis proposed previously [20], which suggests that phosphatization took place soon after (or is coeval with) carbonate sedimentation, dated between 24.9 and 17.8 Ma (Late Oligocene to Early Miocene). Two hypotheses may account for this discrepancy. First, this sample may represent an ancient (Late Cretaceous) phosphorite crust from the Galicia Bank. This interpretation is plausible given that the Galicia Bank has been situated along the northeastern Atlantic margin since the very early stages of ocean opening in this region. Such ancient crusts, indicative of an earlier phosphogenetic event, have also been identified on other seamounts, such as the Tropic Seamount [22]. The formation of Upper Cretaceous phosphorites on the Galicia Bank aligns well with the major Cretaceous phosphogenic event documented globally [35,41]. This correlation suggests that the Galicia Bank was affected by the same large-scale oceanographic and geochemical processes—such as upwelling and sediment condensation—that drove widespread phosphogenesis during this period. Alternatively, the shift toward lower Sr isotope compositions could be explained by the contribution of hydrothermal

fluids interacting with mafic rocks, which typically exhibit low $^{87}Sr/^{86}Sr$ ratios (~0.7030 [99,100]). This scenario would be plausible only if the age of the investigated phosphorite (sample 36DRN) is also Late Oligocene to Early Miocene (considering a similar age for pristine calcite included in the phosphorite [20]. This is unlikely according to [20].

Irrespective of which hypothesis is favored, the observed shift in isotope values and trace element contents between the two P-rich layers of the layered phosphorites would suggest a change in depositional chemistry (as evidenced in Figure 9C), supporting the idea of two distinct phosphogenetic events with contrasted REE sources (influence of pore water fluids or hydrothermal contribution).

For the phosphorites of the Galicia Bank, the initial $^{87}Sr/^{86}Sr$ ratios of the phosphorite slab that is reworked and impregnated with Mn-Fe crusts are significantly more radiogenic than those of contemporaneous Late Oligocene–Early Miocene seawater (Figure 8). This shift toward higher $^{87}Sr/^{86}Sr$ values likely reflects the involvement of younger seawater, postdating the primary phosphorite formation, and possibly coinciding with the development of the Fe-Mn oxides surrounding the slab. In the $\delta^{18}O$ vs. $^{87}Sr/^{86}Sr$ diagram (Figure 8), these isotopic values align well with those of Middle to Upper Miocene phosphates. This suggests that the Fe-Mn crusts may have formed during the Middle–Upper Miocene, potentially in association with a hydrothermal system. Such a system could have been driven by geothermal activity and geochemically influenced by the granodioritic to granitic basement rocks underlying the Galicia Bank. This interaction with radiogenic crust could account for the elevated $^{87}Sr/^{86}Sr$ values, as also proposed previously [20]. Part of the isotopic variability observed in the studied phosphorites from the Galicia Bank reflects later diagenetic overprinting. The coupled shift in $\delta^{18}O$ and $^{87}Sr/^{86}Sr$ values suggests superimposed modification processes affecting both isotopic systems and could support a multi-stage evolution involving initial phosphogenesis (and primary seawater signature), followed by early diagenetic modification and later Fe–Mn overprinting associated with fluid circulation. Interaction with basement-derived fluids, previously proposed for the Galicia Bank [20], may have contributed to the radiogenic Sr enrichment, whereas oxygen isotope variations may additionally reflect temperature-dependent exchange during late-stage alteration.

The phosphorite from the Seine Seamount is notably characterized by a Sr isotope composition that is significantly less radiogenic than that of contemporaneous seawater associated with the main phosphogenetic events during the Eocene and Upper Miocene [45], despite overlapping $\delta^{18}O$ values in samples most enriched in apatite. A plausible explanation for this less radiogenic signature is a volcanic contribution, as volcanic sources typically exhibit low $^{87}Sr/^{86}Sr$ ratios. Support for this volcanic input is provided by the presence of tiny Mg-rich laths within brecciated phosphorite, suggesting the incorporation of volcanic ash into the breccia. Notably, a major phase of explosive basaltic volcanism occurred on the island of Porto Santo—located about 150 km from the Seine Seamount—during the Middle Miocene (14–11 Ma [50]). Porto Santo's geological sequence includes trachytic flows and hyaloclastites overlain by submarine to subaerial basaltic-hawaiitic rocks [101]. These volcanic rocks are marked by low initial $^{87}Sr/^{86}Sr$ ratios (0.70281–0.70295) and are enriched in Ti (up to 3.72 wt% TiO_2 [92]). This volcanic input could account for both the low radiogenic Sr isotopic signature and the elevated Ti content in the Seine Seamount phosphorite. This hypothesis is further supported by the discrimination diagrams shown in Figure 9, where the phosphorites from the Seine Seamount plot near the field defined by the mafic rocks of Porto Santo. This interpretation implies a Middle Miocene age for the phosphorite, rather than an Eocene or Upper Miocene age.

The isotopic results and comparison with previous chronological constraints indicate that the investigated phosphorites record several phosphogenic stages rather than a single mineralization event, reflecting regionally distinct episodes of phosphogenesis and

subsequent overprinting processes. The oldest mineralization is represented by the Late Cretaceous phosphorites preserved at the Tropic Seamount, where U–Pb ages obtained on phosphatized carbonate substrates indicate an age of ~84 Ma [22]. This period corresponds to globally widespread phosphate accumulation associated with high sea level conditions, expanded epicontinental seas and enhanced upwelling activity recognized in many Tethyan and Atlantic domains [35,41,42]. A similarly complex history is recorded at Galicia Bank, where phosphatization affected pre-existing carbonate substrates that may locally preserve Late Cretaceous to early Cenozoic depositional records [20]. More specifically, some phosphorites from the Galicia Bank are interpreted as mineralization episodes related to Late Oligocene–Early Miocene phosphatization. Their isotopic compositions, together with previous studies, indicate later modification processes involving Fe–Mn impregnation and interaction with external fluids. The radiogenic Sr signatures and displacement from the seawater evolution trend suggest that hydrothermal fluids derived from leaching of the Variscan granitic basement may have contributed to secondary alteration [20]. Phosphorite formation at the Galicia Bank and the Seine Seamount during the Early to Middle Miocene aligns with periods of intensified upwelling, similar to that observed in the equatorial Atlantic. For instance, $^{87}Sr/^{86}Sr$ ratios from phosphorites on the Carter and Hirondelle Seamounts (eastern equatorial Atlantic, between 6°N and 9°N) indicate phosphatization of Middle Eocene reef limestones occurred between 16 and 23 Ma [102].

5.3. Genetic Relationships Between Phosphogenesis and Fe–Mn Mineralization and REY Enrichment

The close spatial and temporal association between phosphorites and Fe–Mn deposits suggests that phosphogenesis and Fe–Mn mineralization are genetically interconnected processes rather than independent events. Phosphatization represents a major secondary process affecting both hydrogenetic and diagenetic Fe–Mn deposits and constitutes an important mechanism for REY and CRM enrichment [21,53,103–105]. Hydrogenetic Fe–Mn oxyhydroxides act as highly efficient scavengers of dissolved trace elements, particularly beneath the oxygen minimum zone (OMZ). Their high specific surface area and strong adsorption capacity enable the effective removal of REYs and phosphorus from seawater [21,24,26].

During phosphatization, redox-driven dissolution of Mn oxides and partial destabilization of Fe phases may release phosphorus into pore waters, thereby promoting authigenic carbonate fluorapatite precipitation and inducing redistribution of REYs between phosphatic and oxide reservoirs [106,107]. These processes likely develop under less oxic conditions than those prevailing during primary hydrogenetic crust growth and commonly result in dissolution–recrystallisation textures and epigenetic carbonate fluorapatite impregnation [103,104]. Consequently, phosphogenesis may locally represent a secondary overprint affecting pre-existing Fe–Mn mineralization rather than a strictly synchronous process.

Comparable relationships have been documented in several Atlantic domains. At the Galicia Bank, phosphorite hardgrounds, Mn impregnation layers, Co-rich nodules and hydrogenetic Fe–Mn crusts form a complex paragenetic sequence reflecting successive phosphatization episodes, hydrothermal inputs and later hydrogenetic growth stages [20]. Similarly, at Tropic Seamount, phosphatization episodes affecting pre-existing hydrogenetic crusts resulted in carbonate fluorapatite accumulation and partial replacement of Fe–Mn oxides under suboxic conditions, significantly modifying the original Fe–Mn composition and associated geochemical signatures [21,23,53]. The major phosphatization event recognized at ~38 Ma further indicates that phosphogenesis may postdate the initial formation of hydrogenetic crusts and constitute a later diagenetic overprint [22]. In the Canary Island Seamount Province, the influx of Saharan dust, characterized by high Fe and relatively low P contents, enhances seawater fertilization and promotes the

accumulation of Fe-rich hydrogenetic oxyhydroxides in ferromanganese crusts. The development of these Fe- and P-enriched phases constitutes an important precursor to subsequent phosphatization events, during which phosphate minerals partially replace the original Fe–Mn crusts [21,108].

5.4. Controls on CRM Enrichment and Implications for Resource Potential

The investigated phosphorites display marked differences in other CRM enrichments (e.g., REYs, Co, Pt), indicating that phosphogenesis alone was not sufficient to generate economically significant concentrations. The highest REY concentrations occur in phosphorites spatially associated with Fe–Mn oxyhydroxides, suggesting that CRM enrichment results from the interaction of several processes rather than from primary phosphatization alone. Hydrogenetic Fe–Mn phases act as efficient scavengers of REYs and other critical elements from seawater [24,26], whereas subsequent phosphatization and diagenetic redistribution may transfer some of these elements, especially HREEs, into phosphatic phases [48]. Consequently, the strongest enrichments appear to be associated with multiphase mineralization histories involving phosphogenesis, Fe–Mn growth, phosphatization and later overprinting processes.

In contrast, phosphorites formed under dominantly diagenetic conditions and characterized by lesser Fe–Mn mineralization/impregnation generally display lower CRM concentrations despite locally elevated P contents [103]. This observation indicates that phosphorite abundance alone is not a reliable predictor of resource potential and that phosphorus enrichment does not necessarily imply significant CRM accumulation.

The results further suggest that the most prospective deep-sea phosphorites are not necessarily the most phosphatic deposits but rather those combining phosphatization, hydrogenetic Fe–Mn mineralization and evidence for prolonged fluid interaction, repeated enrichment events or secondary redistribution processes. Their economic interest therefore probably resides less in phosphate tonnage alone than in the coexistence of phosphatic and Fe–Mn mineral systems capable of concentrating REYs and other critical elements. In this sense, the diagenetic replacement associated with phosphatization of primary hydrogenetic ferromanganese crusts is identified as a critical factor controlling the concentration and enrichment of Pt in these phosphatized deposits [26].

Despite locally elevated REY concentrations, deep-sea phosphorites associated with Fe–Mn mineralization remain relatively limited in volume compared with the giant shallow-marine phosphorite provinces developed during major phosphogenic episodes, such as those of West Sahara, Tunisia–Algeria and Egypt, which constitute some of the world's largest phosphate resources. West Sahara phosphorites correspond to Upper Cretaceous–Lower Eocene deposits and represent the largest sedimentary phosphate accumulation worldwide, formed in extensive marine environments dominated by phosphogenesis and early diagenetic concentration processes [10]. Tunisian and Algerian phosphorites belong to the Tethyan phosphogenic province and were deposited within Paleocene–Eocene basins surrounding the Kasserine topographic high, where REY concentrations may exceed 1000 ppm and appear strongly controlled by depositional environments and redox conditions [11]. Egyptian phosphorites formed during Campanian–Ypresian phosphogenic events along the southern Tethyan margin and are characterized by microbial mediation and carbonate fluorapatite precipitation [9].

In contrast, the Atlantic phosphorites investigated here occur as smaller deposits associated with Fe–Mn mineralization on seamounts. Although their tonnage is likely more limited than that of giant Tethyan phosphorite provinces, they locally display comparable enrichment mechanisms involving phosphogenesis, secondary redistribution and interaction with Fe–Mn oxyhydroxides. Recently, the GSEU consortium project estimated resources of approximately 14.9 million tons of phosphate rock and 6500 tons of REYs at the summit of

Tropic Seamount [36]. Consequently, the phosphorites investigated in this study should probably not be considered direct equivalents of large sedimentary phosphorite provinces but rather complementary phosphate-related CRM targets and valuable natural laboratories for understanding the mechanisms controlling marine REY enrichment.

6. Conclusions and Prospects

This study provides a detailed petrographic, geochemical, and isotopic characterization of deep-sea phosphorites from the Galicia Bank, Madeira, and Canary seamounts, elucidating their formation history and CRM potential. The REE patterns, Ce anomalies, and Y/Ho ratios indicate that phosphogenesis occurred near the suboxic/oxic boundary, with contributions from seawater, modified porewaters, diagenesis, and, locally, volcanic (and possibly hydrothermal) sources. Layer-specific REE signatures within individual phosphorite bodies in the Galicia Bank phosphorite further reflect temporal and geochemical heterogeneities during apatite precipitation.

In situ O and Sr isotope analyses constrain the timing of phosphatization events from the Upper Cretaceous to the Miocene, which are connected to major phosphogenetic events related to upwelling. These data reveal both primary mineralization and subsequent overprints linked to Fe-Mn oxide formation (on the Tropic Seamount and the Galicia Bank) or volcanic input (at the Seine Seamount). These isotopic systems effectively differentiate between syndepositional and post-depositional processes, supporting the interpretation of multiphase phosphogenesis across the study area.

The variability observed in REE distributions and Sr isotope compositions highlights the complex diagenetic and post-diagenetic processes influencing phosphorite–ferromanganese systems. This complexity has direct implications for the CRM potential of these deposits. First, the phosphorites themselves constitute primary reservoirs of phosphorus and fluorine, and potentially of REYs, particularly in locations like the Galicia Bank and Seine Seamount—provided that resource estimates in the tens to hundreds of millions of tonnes can be substantiated. However, accurately estimating the scale of these resources remains a significant challenge. Second, these findings may be particularly relevant in environments where phosphatization affects the trace metal retention capacity of Mn-oxide phases. In such settings, the use of high-resolution imaging, trace element mapping, and in situ isotopic techniques is essential for reconstructing the history of phosphogenesis and for evaluating the economic viability of these deep-sea mineral systems.

Supplementary Materials: The following supporting information can be downloaded at: https://www.mdpi.com/article/10.3390/min16060661/s1, Supplementary Material 1—Table S1: Microprobe analyses (oxides in wt.%) of apatite. The detection limit considered is 0.05 wt.%; (-) in the table corresponds to analyses below detection limit. The formulae are calculated to 12.5 O; Table S2: SIMS O isotope data of apatite; Table S3: LA-ICPMS: Sr isotope data of apatite; Supplementary Material S2: Detailed analytical protocol for LA-ICPMS analyses.

Author Contributions: Conceptualization, S.D., F.J.G., V.H.M., N.C., E.T.M. and J.-M.B.; Methodology, S.D., N.C., E.T.M., J.-M.B. and E.D.; Software, S.D., N.C., E.T.M. and E.D.; Validation, S.D., N.C., E.T.M. and E.D.; Formal analysis, S.D., N.C., E.T.M., J.-M.B. and E.D.; Investigation, S.D., F.J.G., E.M., E.S., V.H.M., N.C., E.T.M., J.-M.B. and E.D.; Resources, S.D., F.J.G. and V.H.M.; Data curation, S.D., N.C. and E.D.; Writing—original draft preparation, S.D., F.J.G., E.M., E.S., V.H.M., N.C., E.T.M., J.-M.B. and E.D.; Writing—review and editing, S.D., F.J.G., E.M., E.S., V.H.M., N.C., E.T.M., J.-M.B. and E.D.; Visualization, S.D., F.J.G., E.M., E.S., V.H.M., N.C., E.T.M. and E.D.; Supervision, S.D. and F.J.G.; Project administration, S.D. and F.J.G.; Funding acquisition, S.D., F.J.G., N.C., E.T.M. and E.D. All authors have read and agreed to the published version of the manuscript.

Funding: This work is part of the GSEU—Geological Service for Europe project (through its WP2: Critical Raw Materials, the International Centre of Excellence and the United Nations Framework Classification), which has received funding from the European Union's Horizon Europe research and innovation program under Grant Agreement HORIZON-CL5-2021-D3-02-14, Project 101075609. This work is a contribution to the Spanish State Investigation Agency, project ATLANTIS ((PID2021-124553OB-I00) and the European project TRIDENT (Grant agreement ID: 101091959). Part of the analyses for this study were performed in the Norwegian Laboratory for Mineral and Materials Characterisation (MiMaC) NGU node, supported by the Research Council of Norway project number 269842/F50. The Cameca IMS 1270 E7 ion microprobe at CRPG Nancy is an instrument of the LG-SIMS INSU CNRS national facility.

Data Availability Statement: Data are contained within the article and supplementary materials.

Acknowledgments: The authors would thank Thommy D'heuvaert, Marleen DeCeukelaire and Thomas Goovaerts for the handling and preparation of samples from the collection of the RBINS. The authors thank all the scientific and technical staff who participated in the oceanographic cruises of the DIVA-ARTABRIA and Marine-E Tech projects onboard the R/V *Sarmiento de Gamboa* and R/V *James Cook*, respectively, for data acquisition and for their expertise in collecting the samples. The authors would like to sincerely thank the Editorial Committee of *Minerals* and the four anonymous reviewers for their valuable comments and suggestions, which significantly improved the manuscript.

Conflicts of Interest: The authors declare no conflict of interest.

References

1. Föllmi, K.B. The phosphorus cycle, phosphogenesis and marine phosphate-rich deposits. *Earth-Sci. Rev.* **1996**, *40*, 55–124.
2. European Commission. Report on Critical Raw Materials for the EU. Critical Raw Materials Profiles. Available online: http://ec.europa.eu/DocsRoom/documents/11911/attachments/1/translations (accessed on 9 December 2016).
3. European Commission. On the Review of the List of Critical Raw Materials for the EU and the Implementation of the Raw Materials Initiative. Available online: http://eur-lex.europa.eu/legal-content/EN/TXT/PDF/?uri=CELEX:52014DC0297&from=EN (accessed on 9 December 2016).
4. Christmann, P. A forward look into rare earth supply and demand: A role for sedimentary phosphate deposits? *Procedia Eng.* **2014**, *83*, 19–26.
5. Ihlen, P.M.; Schiellerup, H.; Gautneb, H.; Skår, Ø. Characterization of apatite resources in Norway and their REE potential—A review. *Ore Geol. Rev.* **2014**, *58*, 126–147.
6. Emsbo, P.; McLaughlin, P.I.; Breit, G.N.; du Bray, E.A.; Koenig, A.E. Rare earth elements in sedimentary phosphate deposits: Solution to the global REE crisis? *Gondwana Res.* **2015**, *27*, 776–785.
7. Decrée, S.; Coint, N.; Debaille, V.; Hagen-Peter, G.; Leduc, T.; Schiellerup, H. Potential for REE of igneous-related apatite deposits in Europe. In *The Green Stone Age—Exploration and Exploitation of Minerals for Green Technologies*; Hanghøj, K., Smelror, M., Schiellerup, H., Eds.; Geological Society of London: London, UK, 2022.
8. Pereira, F.; Bilal, E. Phosphoric acid extraction and rare earth recovery from apatites of the Brazilian phosphatic ores. *Rom. J. Miner. Depos.* **2012**, *85*, 49–52.
9. Ahmed, E.A.; Kurzweil, J. Sedimentological, mineralogical and geochemical characteristics of Upper Cretaceous Egyptian phosphorites with special reference to the microbial role in phosphogenesis. In *Aspects of Cretaceous Stratigraphy and Palaeobiogeography*; Wagreich, M., Ed.; Österreichische Akademie der Wissenschaften: Vienna, Austria, 2002; Volume 15, pp. 11–34.
10. El Bamiki, R.; Raji, O.; Ouabid, M.; Elghali, A.; Khadiri Yazami, O.; Bodinier, J.L. Phosphate rocks: A review of sedimentary and igneous occurrences in Morocco. *Minerals* **2021**, *11*, 1137.
11. Kechiched, R.; Sinisi, R.; Kocsis, L.; Bruguier, O.; Mongelli, G.; Ferhaoui, S.; Laouar, R. Phosphate deposits in North Africa: An overview of Algerian-Tunisian deposits, geochemistry and paleoenvironments. In *The Geology of North Africa*; Springer: Cham, Switzerland, 2024; pp. 471–499.
12. Cook, P.J.; Shergold, J.H. (Eds.) *Phosphate Deposits of the World. Volume 3: Neogene to Modern Phosphorites*; Cambridge University Press: Cambridge, UK, 1986, 464p.
13. Burnett, W.C.; Riggs, S.R. *Phosphate Deposits of the World*; Cambridge University Press: Cambridge, UK, 1990; 480p.

14. Hein, J.R.; Koschinsky, A.; Mikesell, M.; Mizell, K.; Glenn, C.R.; Wood, R. Marine phosphorites as potential resources for heavy rare earth elements and yttrium. *Minerals* **2016**, *6*, 88.
15. González, F.J.; Medialdea, T.; Schiellerup, H.; Zananiri, I.; Ferreira, P.; Somoza, L.; Monteys, X.; Alcorn, T.; Marino, E.; Lobato, A.B.; et al. MINDeSEA: Exploring seabed mineral deposits in European seas, metallogeny and geological potential for strategic and critical raw materials. *Geol. Soc. Lond. Spec. Publ.* **2023**, *526*, 289–317.
16. Silva, E.; Viegas, D.; Martins, A.; Almeida, J.; Almeida, C.; Neves, B.; Madureira, P.; Wheeler, A.J.; Salavasidis, G.; Phillips, A.; et al. TRIDENT—Technology based impact assessment tool for sustainable, transparent deep sea mining exploration and exploitation: A project overview. In Proceedings of the OCEANS 2023–Limerick, Limerick, Ireland, 5–8 June 2023; pp. 1–7.
17. International Seabed Authority. Available online: https://isa.org.jm/ (accessed on 28 May 2026).
18. Baturin, G.N. *Phosphorites on the Sea Floor*; Developments in Sedimentology; Elsevier: Amsterdam, The Netherlands, 1982; Volume 33, 343p.
19. Hein, J.R.; Manheim, F.T.; Schwab, W.C.; Davis, A.S. Ferromanganese crusts from Necker Ridge, Horizon Guyot and SP Lee Guyot: Geological considerations. *Mar. Geol.* **1985**, *69*, 25–54.
20. González, F.J.; Somoza, L.; Hein, J.R.; Medialdea, T.; León, R.; Urgorri, V.; Martín-Rubí, J.A.; Reyes, J. Phosphorites, Co-rich Mn nodules, and Fe-Mn crusts from Galicia Bank, NE Atlantic: Reflections of Cenozoic tectonics and paleoceanography. *Geochem. Geophys. Geosyst.* **2016**, *17*, 346–374.
21. Marino, E.; González, F.J.; Somoza, L.; Lunar, R.; Ortega, L.; Vázquez, J.T.; Bellido, E. Strategic and rare elements in Cretaceous-Cenozoic cobalt-rich ferromanganese crusts from seamounts in the Canary Island Seamount Province, northeastern tropical Atlantic. *Ore Geol. Rev.* **2017**, *87*, 41–61.
22. Josso, P.; Parkinson, I.; Horstwood, M.; Lusty, P.; Chenery, S.; Murton, B. Improving confidence in ferromanganese crust age models: A composite geochemical approach. *Chem. Geol.* **2019**, *513*, 108–119.
23. Hassan, M.B.; Koschinsky, A.; da Silva, G.L.X.; Dantas, R.C.; Kuhn, T.; Millo, C.; Jovane, L.; Kletetschka, G. Magnetization of ferromanganese crusts: Geochemical and magnetic insights from Rio Grande Rise and Tropic Seamount. *Geochem. Geophys. Geosyst.* **2024**, *25*, e2023GC011210.
24. Hein, J.R.; Mizell, K.; Koschinsky, A.; Conrad, T.A. Deep-ocean mineral deposits as a source of critical metals for high- and green-technology applications: Comparison with land-based resources. *Ore Geol. Rev.* **2013**, *51*, 1–14.
25. Maeno, M.Y.; Ohashi, H.; Yonezu, K.; Miyazaki, A.; Okaue, Y.; Watanabe, K.; Ishida, T.; Tokunaga, M.; Yokoyama, T. Sorption behavior of the Pt(II) complex anion on manganese dioxide, δ-MnO_2: A model reaction to elucidate the mechanism by which Pt is concentrated into a marine ferromanganese crust. *Miner. Depos.* **2016**, *51*, 211–218.
26. Koschinsky, A.; Hein, J.R.; Kraemer, D.; Foster, A.L.; Kuhn, T.; Halbach, P. Platinum enrichment and phase associations in marine ferromanganese crusts and nodules based on a multi-method approach. *Chem. Geol.* **2020**, *539*, 119426.
27. Jarvis, I. Phosphorite geochemistry: State-of-the-art and environmental concerns. *Eclogae Geol. Helv.* **1994**, *87*, 643–700.
28. Shields, G.; Stille, P. Diagenetic constraints on the use of cerium anomalies as palaeoseawater redox proxies: An isotopic and REE study of Cambrian phosphorites. *Chem. Geol.* **2001**, *175*, 29–48.
29. Chen, J.; Algeo, T.J.; Zhao, L.; Chen, Z.Q.; Cao, L.; Zhang, L.; Li, Y. Diagenetic uptake of rare earth elements by bioapatite, with an example from Lower Triassic conodonts of South China. *Earth-Sci. Rev.* **2015**, *149*, 181–202.
30. Wu, W.; Yang, R.; Liu, J.; Wang, Z.; Li, S.; Shao, Y.; Deng, Y.; Ye, T.; Luo, C.; Gao, L.; et al. Origins of the Ediacaran Doushantuo high-grade primary bio-phosphorites at Kaiyang, Guizhou Province, China. *ACS Omega* **2023**, *8*, 47938–47953. https://doi.org/10.1021/acsomega.3c06476.
31. Mei, W.; Cai, C.; Ming, X.; Wang, Z.; Jiang, L. Geochemistry and enrichment of rare earth elements in phosphorite successions in the Lower Cambrian, Eastern Yun'nan, South China. *Minerals* **2025**, *15*, 581.
32. Peng, R.; Yang, R.; Chen, J.; Gao, J.; Gao, L.; Gao, C. Biogenic mineralization controls exceptional rare-earth enrichment in Early Cambrian phosphorites from South China. *Ore Geol. Rev.* **2025**, *178*, 106497.
33. Trappe, J. *Phanerozoic Phosphorite Depositional Systems: A Dynamic Model for a Sedimentary Resource System*; Springer: Berlin/Heidelberg, Germany, 2001; Volume 76, 316p.
34. Brand, U.; Logan, A.; Bitner, M.A.; Griesshaber, E.; Azmy, K.; Buhl, D. What is the ideal proxy of Palaeozoic seawater chemistry? Mem. *Assoc. Australas. Palaeontol.* **2011**, *41*, 9–24.
35. Pufahl, P.K.; Groat, L.A. Sedimentary and igneous phosphate deposits: Formation and exploration: An invited paper. *Econ. Geol.* **2017**, *112*, 483–516.
36. González, F.J.; Marino, E.; GSEU T2.2 Team. *European Offshore CRM Resource Evaluation v1*; GSEU Deliverable D2.7; Geological Service for Europe: Brussels, Belgium, 2025.

37. Balson, P.S. The origin and evolution of Tertiary phosphorites from eastern England. *J. Geol. Soc. Lond.* **1980**, *137*, 723–729.
38. Parrish, J.T. Paleogeographic and paleoclimatic setting of the Miocene phosphogenic episode. In *Phosphate Deposits of the World. Volume 3: Genesis of Neogene to Recent Phosphorites*; Burnett, W.C., Riggs, S.R., Eds.; Cambridge University Press: Cambridge, UK, 1990; pp. 223–240.
39. Jarvis, I. Sedimentology, geochemistry and origin of phosphatic chalks: The Upper Cretaceous deposits of NW Europe. *Sedimentology* **1992**, *39*, 55–97.
40. Jarvis, I. The Santonian-Campanian phosphatic chalks of England and France. *Proc. Geol. Assoc.* **2006**, *117*, 219–237.
41. Lucas, J.; Prévôt-Lucas, L. Tethyan phosphates and bioproductites. In *The Ocean Basins and Margins. Volume 8: The Tethys Ocean*; Nairn, A.E.M., Ed.; Plenum Press: New York, NY, USA, 1995; pp. 367–391.
42. Hashempour, S.S.; Maghfouri, S.; Rastad, E.; González, F.J. Metallogeny and temporal-spatial distribution of sedimentary phosphorite mineralization in Iran, relation to Tethyan oceans evolution and implications for future exploration. *Ore Geol. Rev.* **2024**, *164*, 105855.
43. Basel, B.V. Phosphorus and phosphorites: Sedimentology and environments of formation. *Eclogae Geol. Helv.* **1994**, *87*, 747–788.
44. Riggs, S.R.; Sheldon, R.P. Paleoceanographic and paleoclimatic controls of the temporal and geographic distribution of Upper Cenozoic continental margin sediments of the southeastern United States. In *Phosphate Deposits of the World. Volume 3: Neogene to Modern Phosphorites*; Burnett, W.C., Riggs, S.R., Eds.; Cambridge University Press: Cambridge, UK, 1990; pp. 53–76.
45. Koschinsky, A.; Halbach, P.; Hein, J.R.; Mangini, A. Ferromanganese crusts as indicators for paleoceanographic events in the NE Atlantic. *Geol. Rundsch.* **1996**, *85*, 567–576.
46. Geldmacher, J.; Hoernle, K.; van den Bogaard, P.; Duggen, S.; Werner, R. New 40Ar/39Ar age and geochemical data from seamounts in the Canary and Madeira volcanic provinces: Support for the mantle plume hypothesis. Earth Planet. *Sci. Lett.* **2005**, *237*, 85–101.
47. Marino, E.; González, F.J.; Lunar, R.; Reyes, J.; Medialdea, T.; Castillo-Carrión, M.; Somoza, L. High-resolution analysis of critical minerals and elements in Fe–Mn crusts from the Canary Island Seamount Province, Atlantic Ocean. *Minerals* **2018**, *8*, 285.
48. Muinos, S.B. Ferromanganese Crusts from the Seamounts North of Madeira Island: Composition, Origin and Paleoceanographic Conditions. Ph.D. Thesis, Kiel University, Kiel, Germany, 2015.
49. Muinos, S.B.; Hein, J.R.; Frank, M.; Monteiro, J.H.; Gaspar, L.; Conrad, T.; Abrantes, F. Deep-sea Fe-Mn crusts from the northeast Atlantic Ocean: Composition and resource considerations. *Mar. Georesour. Geotechnol.* **2013**, *31*, 40–70.
50. Merle, R.; Jourdan, F.; Girardeau, J. Geochronology of the Tore-Madeira Rise seamounts and surrounding areas: A review. *Aust. J. Earth Sci.* **2018**, *65*, 591–605.
51. Palomino, D.; Vázquez, J.T.; Somoza, L.; León, R.; López-González, N.; Medialdea, T.; Rengel, J.A.; Fernández-Salas, L.-M.; González, F.-J. Geomorphological features in the southern Canary Island Volcanic Province: The importance of volcanic processes and massive slope instabilities associated with seamounts. *Geomorphology* **2016**, *255*, 125–139.
52. Kfouri, L.O.; Millo, C.; de Lima, A.E.; Silveira, C.S.; Sant'Anna, L.G.; Marino, E.; González, F.J.; Sayeg, I.J.; Hein, J.R.; Jovane, L.; et al. Growth of ferromanganese crusts on bioturbated soft substrate, Tropic Seamount, northeast Atlantic Ocean. *Deep Sea Res. Part. I Oceanogr. Res. Pap.* **2021**, *175*, 103586.
53. Marino, E.; González, F.J.; Kuhn, T.; Madureira, P.; Wegorzewski, A.V.; Mirão, J.; Medialdea, T.; Oeser, M.; Miguel, C.; Reyes, J.; et al. Hydrogenetic, diagenetic and hydrothermal processes forming ferromanganese crusts in the Canary Island Seamounts and their influence in the metal recovery rate with hydrometallurgical methods. *Minerals* **2019**, *9*, 439.
54. Josso, P.; Lusty, P.; Chenery, S.; Murton, B. *Goldschmidt 2021 Abstract*; European Association of Geochemistry: Clermont-Ferrand, France, 2021. https://doi.org/10.7185/gold2021.6110.
55. Medri, A. Mineralogy and Geochemistry of Phosphorite Deposits from Tropic Seamount, NE Tropical Atlantic Ocean. Master's Thesis, Università di Bologna, Bologna, Italy, 2022.
56. van den Bogaard, P. The origin of the Canary Island Seamount Province—New ages of old seamounts. *Sci. Rep.* **2013**, *3*, 2107.
57. Harmon, R.S.; Lawley, C.J.; Watts, J.; Harraden, C.L.; Somers, A.M.; Hark, R.R. Laser-induced breakdown spectroscopy—An emerging analytical tool for mineral exploration. *Minerals* **2019**, *9*, 718.
58. Baele, J.M.; Bouzahzah, H.; Papier, S.; Decrée, S.; Verheyden, S.; Burlet, C.; Dejonghe, L. Trace-element imaging at macroscopic scale in a Belgian sphalerite–galena ore using laser-induced breakdown spectroscopy (LIBS). *Geol. Belg.* **2021**, *24*, 125–137.
59. Coron, J.; Papier, S.; Decrée, S.; Ferreira, V.; Duponchel, L.; Baele, J.M. Investigating critical metals Ge and Ga in complex sulphide mineral assemblages using LIBS mapping. *Spectrochim. Acta Part B At. Spectrosc.* **2024**, *219*, 107004.
60. Paton, C.; Hellstrom, J.; Paul, B.; Woodhead, J.; Hergt, J. Iolite: Freeware for the visualisation and processing of mass spectrometric data. *J. Anal. At. Spectrom.* **2011**, *26*, 2508–2518.

61. Longerich, H.P.; Jackson, S.E.; Günther, D. Laser ablation inductively coupled plasma mass spectrometric transient signal data acquisition and analyte concentration calculation. *J. Anal. At. Spectrom.* **1996**, *11*, 899–904.
62. Žigaitė, Ž.; Whitehouse, M. Stable oxygen isotopes of dental biomineral: Differentiation at the intra- and inter-tissue level of modern shark teeth. *GFF* **2014**, *136*, 337–340.
63. Chen, J.; Shen, S.Z.; Li, X.H.; Xu, Y.G.; Joachimski, M.M.; Bowring, S.A.; Erwin, D.H.; Yuan, D.-X.; Chen, B.; Zhang, H.; et al. High-resolution SIMS oxygen isotope analysis on conodont apatite from South China and implications for the end-Permian mass extinction. *Palaeogeogr. Palaeoclim. Palaeoecol.* **2016**, *448*, 26–38.
64. Emo, R.B.; Smit, M.A.; Schmitt, M.; Kooijman, E.; Scherer, E.E.; Sprung, P.; Bleeker, W.; Mezger, K. Evidence for evolved Hadean crust from Sr isotopes in apatite within Eoarchean zircon from the Acasta Gneiss Complex. *Geochim. Cosmochim. Acta* **2018**, *235*, 450–462.
65. Li, Z.; Duan, D.; Jiang, S.; Ma, Y.; Yuan, H. In situ analysis of major elements, trace elements and Sr isotopic compositions of apatite from the granite in the Chengchao skarn-type Fe deposit, Edong ore district: Implications for petrogenesis and mineralization. *J. Earth Sci.* **2018**, *29*, 295–306.
66. Yang, J.H.; Kang, L.F.; Peng, J.T.; Zhong, H.; Gao, J.F.; Liu, L. In situ elemental and isotopic compositions of apatite and zircon from the Shuikoushan and Xihuashan granitic plutons: Implication for Jurassic granitoid-related Cu-Pb-Zn and W mineralization in the Nanling Range, South China. *Ore Geol. Rev.* **2018**, *93*, 382–403.
67. Wotte, T.; Skovsted, C.B.; Whitehouse, M.J.; Kouchinsky, A. Isotopic evidence for temperate oceans during the Cambrian Explosion. *Sci. Rep.* **2019**, *9*, 6330.
68. Yang, Q.; Xia, X.P.; Zhang, L.; Zhang, W.; Zhang, Y.; Chen, L.; He, M.; Yang, Y. Oxygen isotope homogeneity assessment for apatite U-Th-Pb geochronology reference materials. *Surf. Interface Anal.* **2019**, *52*, 197–213.
69. McArthur, J.M.; Howarth, R.J. Strontium isotope stratigraphy of the Cretaceous. *Geol. Soc. Lond. Spec. Publ.* **2025**, *544*, SP544-2023-85.
70. Decrée, S.; Pasava, J.; Baele, J.M.; Mercadier, J.; Rösel, D.; Frimmel, H. In-situ trace element and Sr isotope signature of apatite: A new key to unravelling the genesis of polymetallic mineralisation in black shales, Early Cambrian Niutitang Formation, Southern China. *Ore Geol. Rev.* **2022**, *150*, 105130.
71. Decrée, S.; Deloule, E.; Barros, R.; Mercadier, J.; Höhn, S.; Peiffert, C.; Baele, J.M. Processes controlling rare earth element distribution in sedimentary apatite: Insights from spectroscopy, in situ geochemistry and O and Sr isotope composition. *Sedimentology* **2024**, *71*, 713–744.
72. Edwards, C.T.; Jones, C.M.; Quinton, P.C.; Fike, D.A. Oxygen isotope ($\delta^{18}O$) trends measured from Ordovician conodont apatite using SIMS: Implications for paleothermometry. *GSA Bull.* **2022**, *134*, 261–274.
73. Trotter, J.A.; Williams, I.S.; Barnes, C.R.; Lécuyer, C.; Nicoll, R.S. Did cooling oceans trigger Ordovician biodiversification? Evidence from conodont thermometry. *Science* **2008**, *321*, 550–554.
74. Mulder, J.; Hagen-Peter, G.; Ubide, T.; Andreasen, R.; Kooijman, E.; Kielman-Schmitt, M.; Feng, Y.; Paul, B.; Karlsson, A.; Tegner, C.; et al. New reference materials, analytical procedures and data reduction strategies for Sr isotope measurements in geological materials by LA-MC-ICP-MS. *Geostand. Geoanal. Res.* **2023**, *47*, 311–336.
75. Condie, K.C. Chemical composition and evolution of the upper continental crust: Contrasting results from surface samples and shales. *Chem. Geol.* **1993**, *104*, 1–37.
76. Burke, W.H.; Denison, R.E.; Hetherington, E.A.; Koepnick, R.B.; Nelson, H.F.; Otto, J.B. Variation of seawater 87Sr/86Sr throughout Phanerozoic time. *Geology* **1982**, *10*, 516–519.
77. Pucéat, E.; Lécuyer, C.; Donnadieu, Y.; Naveau, P.; Cappetta, H.; Ramstein, G.; Kriwet, J. Fish tooth $\delta^{18}O$ revising Late Cretaceous meridional upper ocean water temperature gradients. *Geology* **2007**, *35*, 107–110.
78. Veizer, J. Strontium isotopes in seawater through time. *Annu. Rev. Earth Planet. Sci.* **1989**, *17*, 141–167.
79. Lécuyer, C.; Grandjean, P.; O'Neil, J.R.; Cappetta, H.; Martineau, F. Thermal excursions in the ocean at the Cretaceous–Tertiary boundary, northern Morocco: $\delta^{18}O$ record of phosphatic fish debris. *Palaeogeogr. Palaeoclima. Palaeoecol.* **1993**, *105*, 235–243.
80. Longinelli, A.; Iacumin, P.; Ramigni, M. $\delta^{18}O$ of carbonate, quartz and phosphate from belemnite guards: Implications for the isotopic record of old fossils and the isotopic composition of ancient seawater. Earth Planet. *Sci. Lett.* **2002**, *203*, 445–459.
81. Ounis, A.; Kocsis, L.; Chaabani, F.; Pfeifer, H.R. Rare earth elements and stable isotope geochemistry, $\delta^{13}C$ and $\delta^{18}O$, of phosphorite deposits in the Gafsa Basin, Tunisia. *Palaeogeogr. Palaeoclim. Palaeoecol.* **2008**, *268*, 1–18.
82. Vennemann, T.W.; Hegner, E. Oxygen, strontium, and neodymium isotope composition of fossil shark teeth as a proxy for the palaeoceanography and palaeoclimatology of the Miocene northern Alpine Paratethys. *Palaeogeogr. Palaeoclim. Palaeoecol.* **1998**, *142*, 107–121.

83. Kocsis, L.; Vennemann, T.W.; Hegner, E.; Fontignie, D.; Tütken, T. Constraints on Miocene oceanography and climate in the Western and Central Paratethys: O-, Sr-, and Nd-isotope compositions of marine fish and mammal remains. *Palaeogeogr. Palaeoclim. Palaeoecol.* **2009**, *271*, 117–129.
84. Pan, Y.; Fleet, M.E. Compositions of the apatite-group minerals: Substitution mechanisms and controlling factors. *Rev. Mineral. Geochem.* **2002**, *48*, 13–49.
85. McArthur, J.M.; Walsh, J.N. Rare-earth geochemistry of phosphorites. *Chem. Geol.* **1984**, *47*, 191–220.
86. Lécuyer, C.; Reynard, B.; Grandjean, P. Rare earth element evolution of Phanerozoic seawater recorded in biogenic apatites. *Chem. Geol.* **2004**, *204*, 63–102.
87. Ye, Y.; Wang, H.; Wang, X.; Zhai, L.; Wu, C.; Zhang, S. Elemental geochemistry of lower Cambrian phosphate nodules in Guizhou Province, South China: An integrated study by LA-ICP-MS mapping and solution ICP-MS. *Palaeogeogr. Palaeoclim. Palaeoecol.* **2020**, *538*, 109459.
88. Chen, D.; Wang, J.; Qing, H.; Yan, D.; Li, R. Hydrothermal venting activities in the Early Cambrian, South China: Petrological, geochronological and stable isotopic constraints. *Chem. Geol.* **2009**, *258*, 168–181.
89. Yan, H.; Pi, D.; Xu, L.; Sun, K. The perturbation of the Guadalupian marine environment triggered by early-stage eruption of the Emeishan Large Igneous Province: Rare earth element and Sr-Nd isotope evidence from Zunyi manganese deposit, South China. *Minerals* **2023**, *13*, 965.
90. Gromet, L.P.; Haskin, L.A.; Korotev, R.L.; Dymek, R.F. The "North American shale composite": Its compilation, major and trace element characteristics. *Geochim. Cosmochim. Acta* **1984**, *48*, 2469–2482.
91. Haley, B.A.; Klinkhammer, G.P.; McManus, J. Rare earth elements in pore waters of marine sediments. *Geochim. Cosmochim. Acta* **2004**, *68*, 1265–1279.
92. Kim, J.H.; Torres, M.E.; Haley, B.A.; Kastner, M.; Pohlman, J.W.; Riedel, M.; Lee, Y.J. The effect of diagenesis and fluid migration on rare earth element distribution in pore fluids of the northern Cascadia accretion margin. *Chem. Geol.* **2012**, *291*, 152–165.
93. Geldmacher, J.; Hoernle, K. The 72 Ma geochemical evolution of the Madeira hotspot, eastern North Atlantic: Recycling of Paleozoic ≤500 Ma oceanic lithosphere. *Earth Planet. Sci. Lett.* **2000**, *183*, 73–92.
94. Martin, E.E.; Haley, B.A. Fossil fish teeth as proxies for seawater Sr and Nd isotopes. *Geochim. Cosmochim. Acta* **2000**, *64*, 835–847.
95. Kohn, M.J.; Cerling, T.E. Stable isotope compositions of biological apatite. *Rev. Miner. Geochem.* **2002**, *48*, 455–488.
96. Quinton, P.C.; Law, S.; MacLeod, K.G.; Herrmann, A.D.; Haynes, J.T.; Leslie, S.A. Testing the early Late Ordovician cool-water hypothesis with oxygen isotopes from conodont apatite. *Geol. Mag.* **2017**, *155*, 1727–1741.
97. Drummond, J.B.; Pufahl, P.K.; Porto, C.G.; Carvalho, M. Neoproterozoic peritidal phosphorite from the Sete Lagoas Formation, Brazil, and the Precambrian phosphorus cycle. *Sedimentology* **2015**, *62*, 1978–2008.
98. Hein, J.R.; Yeh, H.W.; Gunn, S.H.; Sliter, W.V.; Benninger, L.M.; Wang, C.H. Two major Cenozoic episodes of phosphogenesis recorded in equatorial Pacific seamount deposits. *Paleoceanography* **1993**, *8*, 293–311.
99. Von Damm, K.L. Seafloor hydrothermal activity: Black smoker chemistry and chimneys. *Annu. Rev. Earth Planet. Sci.* **1990**, *18*, 173–204.
100. Jones, C.E.; Jenkyns, H.C. Seawater strontium isotopes, oceanic anoxic events, and seafloor hydrothermal activity in the Jurassic and Cretaceous. *Am. J. Sci.* **2001**, *301*, 112–149.
101. Schmidt, R.; Schmincke, H.U. From seamount to oceanic island, Porto Santo, central East-Atlantic. *Int. J. Earth Sci.* **2002**, *91*, 594–614.
102. Jones, E.J.W.; BouDagher-Fadel, M.K.; Thirlwall, M.F. An investigation of seamount phosphorites in the Eastern Equatorial Atlantic. *Mar. Geol.* **2002**, *183*, 143–162.
103. Koschinsky, A.; Stascheit, A.; Bau, M.; Halbach, P. Effects of phosphatization on the geochemical and mineralogical composition of marine ferromanganese crusts. *Geochim. Cosmochim. Acta* **1997**, *61*, 4079–4094.
104. Halbach, P.E.; Jahn, A.; Cherkashov, G. Marine Co-rich ferromanganese crust deposits: Description and formation, occurrences and distribution, estimated world-wide resources. In *Deep-Sea Mining: Resource Potential, Technical and Environmental Considerations*; Sharma, R., Ed.; Springer International Publishing: Cham, Switzerland, 2017; pp. 65–141.
105. Huang, S.; Fu, Y. Enrichment characteristics and mechanisms of critical metals in marine Fe-Mn crusts and nodules: A review. *Minerals* **2023**, *13*, 1532.
106. Glasby, G.P.; Schulz, H.D. Eh-pH diagrams for Mn, Fe, Co, Ni, Cu and As under seawater conditions: Application of two new types of Eh-pH diagrams to the study of specific problems in marine geochemistry. *Aquat. Geochem.* **1999**, *5*, 227–248.

107. Schulz, H.D.; Zabel, M. (Eds.) *Marine Geochemistry*, 2nd ed.; Springer: Berlin/Heidelberg, Germany, 2006.
108. Marino, E.; González, F.J.; Kuhn, T.; Madureira, P.; Somoza, L.; Medialdea, T.; Lobato, A.; Miguel, C.; Reyes, J.; Oeser, M. Factors controlling rare earth element plus yttrium enrichment in FeMn crusts from Canary Islands Seamounts (NE Central Atlantic). *Mar. Geol.* **2023**, *464*, 107144. https://doi.org/10.1016/j.margeo.2023.107144.